Microphysics regimes due to haze-cloud interactions: cloud oscillation and cloud collapse

Fan Yang[1], Hamed Fahandezh Sadi[2], Raymond A. Shaw[2], Fabian Hoffmann[3], Pei Hou[2], Aaron Wang[4], and Mikhail Ovchinnikov[4]

[1]Brookhaven National Laboratory, Upton, New York, USA
[2]Michigan Technological University, Houghton, Michigan, USA
[3]Ludwig-Maximilians-Universität München, Munich, Germany
[4]Pacific Northwest National Laboratory, Richland, Washington, USA

Correspondence: Fan Yang (fanyang@bnl.gov)

Abstract. It is known that aqueous haze particles can be activated to cloud droplets in a supersaturated environment. However, haze-cloud interactions have not been fully explored because, among other things, haze particles are not represented in most cloud-resolving models. Here, we conduct a series of large-eddy simulations of a cloud in a convection chamber using a haze-capable Eulerian-based bin microphysics scheme to explore haze-cloud interactions over a wide range of aerosol injection
5 rates. Results show that at low aerosol injection rates (i.e., clean conditions), the cloud exists in a *slow microphysics* regime where cloud response is slow compared to the environmental change and droplet deactivation is negligible. At moderate aerosol injection rates (i.e., polluted conditions), the cloud is in a *fast microphysics* regime where cloud response is fast compared to the environmental change and haze-cloud interactions are important. The increase in liquid water mixing ratio with aerosol injection rate agrees well with the scaling law predicted by a previous theoretical study of these two microphysics regimes.
10 More interestingly, two other microphysics regimes are observed at high aerosol injection rates: *cloud oscillation* and *cloud collapse*. Cloud oscillation occurs as a result of competition between haze and cloud droplets that lead to synchronized droplet activation/deactivation, while cloud collapse happens under weaker forcing of supersaturation where the chamber transfers cloud droplet to haze particles efficiently, leading to a significant decrease (collapse) of cloud droplet number concentration. Results from a box model using a particle-based microphysics approach show similar transitions across microphysics regimes
15 – from slow microphysics, to fast microphysics, and then to cloud oscillation – confirming that cloud oscillation arises from complex interactions between haze and cloud droplets in a turbulent cloud. One special case of cloud collapse leading to a haze-only regime, occurs at extremely high aerosol injection rates, where the sedimentation of haze particles is balanced by the aerosol injection rate, without cloud droplet activation contributing substantially. Our results suggest that haze particles and their interactions with the cloud should be considered especially in polluted conditions, like fog or clouds close to the source
20 of intense natural and anthropogenic aerosol emissions, or in highly dissipated clouds when droplet deactivation is important.

1 Introduction

Atmospheric clouds play an important role in Earth's radiation balance and hydrological cycle. Their optical properties and precipitation efficiency are strongly influenced by the cloud microphysical composition (e.g., droplet size and concentration) and processes (e.g., droplet formation and growth). It is known that cloud droplets in the atmosphere grow from aerosol particles, most of which contain water-soluble materials, such as sodium chloride or ammonium sulfate. Those water-soluble aerosol particles first absorb water vapor in a subsaturated environment to become aqueous droplets (known as haze particles) through deliquescence. Haze particles can then be activated to cloud droplets in a sufficiently supersaturated environment (i.e., when relative humidity is higher than 100%). The supersaturation needed to activate cloud droplets depends on aerosol properties as explained by Köhler theory (Twomey, 1959). Changes in aerosol properties from various anthropogenic and natural emissions can have a significant impact on clouds, thereby exerting a considerable influence on the climate system. So far, aerosol-cloud interaction remains one of the largest uncertainties in our understanding of the climate, partially due to the poor representation of cloud microphysical processes in models and incomplete understanding of those processes at the fundamental level (Morrison et al., 2020).

It is challenging to isolate the impact of aerosol on cloud properties and evolution in the real atmosphere, because cloud microphysics, dynamics and thermodynamics are coupled in a complex way. In addition, cloud properties vary in time and space, making them difficult to thoroughly sample and interpret. In contrast, the Michigan Tech convection cloud chamber, also known as the Pi chamber, can maintain a steady state cloud for several hours under well-controlled initial and boundary conditions (Chang et al., 2016). The Pi chamber creates a well-mixed supersaturated environment by maintaining a warm, humid bottom surface and a cool, humid top surface through Rayleigh-Bénard convection. The cloud is formed by continuously injecting aerosol particles in the supersaturated environment of the cloud chamber, and the cloud can reach a steady state when the droplet activation rate is balanced by the droplet sedimentation rate. Cloud properties are controlled by aerosol properties (e.g., aerosol size, chemical composition, and injection rate) and boundary conditions (e.g., top and bottom temperatures – the driving factor to create a supersaturated environment). Steady-state cloud properties in the Pi chamber, able to be measured in great detail, can be modified by changing aerosol injection rates, providing a unique opportunity to explore aerosol-cloud-turbulence interactions in well-controlled environments.

Pi chamber experiments have shown that increasing aerosol injection rates result in higher cloud droplet number concentrations, smaller mean droplet radii, and narrower droplet size distributions (Chandrakar et al., 2016). Those trends are consistent with results from cloud-resolving large-eddy simulations of the Pi chamber (Thomas et al., 2019). Krueger (2020) derived an analytical expression for the equilibrium cloud droplet size distribution in a turbulent cloud chamber with the assumption of uniform supersaturation. This analytic droplet size distribution, along with three others that account for fluctuations in different ways, have been compared with measured droplet size distributions in the Pi chamber (Chandrakar et al., 2020). Results show that all four analytical droplet size distributions match the observed distribution reasonably well for monodisperse aerosol injection. However, none of them matched well for polydisperse aerosol injections, possibly due to the Ostwald ripening effect (Korolev, 1995; Jensen and Nugent, 2017; Yang et al., 2018), which is not considered in those analytical models. Shaw et al.

55   (2023) developed a theoretical model to describe the microphysical state in cloudy Rayleigh-Bénard convection. The model predicts that $N_d \sim n_{in}$ and $q_l \sim n_{in}$ in the *slow microphysics* regime (i.e., at low aerosol injection rates), while $N_d \sim n_{in}^{5/3}$ and $q_l \sim n_{in}^{2/3}$ in the *fast microphysics* regime (i.e., at high aerosol injection rates), where N_d is the droplet number concentration, n_{in} aerosol injection rate, and q_l liquid water mixing ratio. The slow microphysics regime refers to a relatively clean condition where the cloud would response slowly to an environmental change, while the fast microphysics regime refers to

60   a relatively polluted condition where the cloud would respond quickly to an environmental change. Pi chamber observations confirm the nonlinear relationship between q_l and n_{in} in the fast microphysics regime (see Fig. 7 in Shaw et al., 2023), but more investigations are needed to evaluate the theory and its ability to represent microphysical properties in a convection cloud chamber.

        Besides cloud droplets, observations using a digital optical particle counter show the existence of haze particles with diam-

65   eters down to 0.6 μm (detection limit) in the Pi chamber (Prabhakaran et al., 2020). Results from direct numerical simulations with Lagrangian aerosol/droplet microphysics show that haze particles can be activated and deactivated multiple times in a convection chamber (MacMillan et al., 2022). However, previous theoretical studies do not include haze activation process for simplification (Krueger, 2020; Chandrakar et al., 2020; Shaw et al., 2023). In addition, most previous Pi chamber simulations do not fully resolve haze particles, because in those simulations as well as in most atmospheric cloud simulations, droplets are

70   formed directly from aerosol particles based on Twomey-type activation parameterizations (Twomey, 1959), in which aerosol is activated as a cloud droplet if the environmental supersaturation is larger than a critical supersaturation (Thomas et al., 2019; Grabowski, 2020). Recently, Yang et al. (2023) developed a haze-capable bin microphysics scheme to simulate the Pi chamber by directly calculating the condensational growth of haze and cloud droplets, which naturally resolves droplet activation process without further parameterization. Simulations using this haze-capable bin scheme can capture haze droplet size distri-

75   butions which show a good agreement with simulations from a Lagrangian microphysics scheme, with the latter serving as the "truth" because it does not suffer numerical diffusion during droplet growth and advection (Morrison et al., 2018; Grabowski et al., 2019). Results also show that the simulated cloud properties using the haze-capable bin microphysics scheme agree reasonably well with those using Twomey-type activation. We refer to the Twomey-type activation scheme as the CCN-based bin microphysics scheme, because it treats dry aerosols as Cloud Condensation Nuclei (CCN) which behave like cloud droplets im-

80   mediately after the environmental supersaturation is larger than a critical supersaturation (i.e., without resolving the growth of haze particles). A good agreement between the haze-capable and CCN-based bin microphysics schemes suggests that if we are only interested in the cloud microphysical properties, we could still use Twomey-type activation parameterizations. However, only two aerosol injection rates were used in Yang et al. (2023), and thus, it is not clear whether results from the CCN-based bin microphysics scheme will always be similar to those from the haze-capable bin microphysics scheme, especially in a low

85   supersaturation environment when haze-cloud interaction is important (e.g., Prabhakaran et al., 2020).

        In this study, we conduct a series of large-eddy simulations of the Pi chamber using both CCN-based and haze-capable bin microphysics schemes over a wide range of aerosol injection rates. We aim to address the following questions:

        (a) How do cloud microphysical properties change over a wide range of aerosol injection rates (for constant boundary conditions)?

(b) Do simulation results agree with previous theoretical studies?

(c) How important are haze-cloud interactions in the Pi chamber as well as in natural clouds?

Specifically, related to the question (a), we want to explore how the steady-state supersaturation, mean droplet radius, N_d, and q_l change with aerosol injection rate. For the question (b), we want to evaluate steady-state droplet size distribution predicted in Krueger (2020) and Chandrakar et al. (2020), as well as slow and fast microphysics regimes predicted in Shaw et al. (2023). Related to question (c), we want to know whether cloud properties simulated by the CCN-based bin microphysics scheme are always consistent with those from the haze-capable bin microphysics scheme, as indicated by Yang et al. (2023), or if haze-capable microphysics must be used for certain atmospheric conditions. Note that the Pi chamber could be connected to some simple cloud systems like fog or non-drizzling shallow layer clouds. So what we learn about haze-cloud interactions can be transferred. We want to understand the conditions under which haze-cloud interactions become important, connecting our work to a broader atmospheric science context.

2 Model description and setup

The large-eddy simulation model we use is SAM-Chamber, which is an adapted and modified version of the System for Atmospheric Modeling (SAM, Khairoutdinov and Randall, 2003) to conduct Pi chamber simulations. Major changes in SAM are the consideration of four side walls and the top surface to represent the chamber (detailed in Thomas et al., 2019). SAM-Chamber has been used to simulate the Pi chamber to explore several topics, including the impact of various bin microphysics and advection schemes on Pi chamber simulations (Yang et al., 2022), impact of supersaturation fluctuations on droplet formation and growth (Prabhakaran et al., 2022; Anderson et al., 2023), development of a haze-capable microphysics scheme (Yang et al., 2023), and investigation of drizzle initiation in larger convection chambers (Thomas et al., 2023; Wang et al., 2024). The SAM-Chamber employed in this study is the one used in Wang et al. (2024), where the wall fluxes of momentum, sensible heat, and moisture are modeled in accordance with Monin-Obukhov Similarity Theory (MOST, Monin and Obukhov, 1954) as before but with the following changes: (1) The roughness lengths for momentum (z_0), sensible heat (z_t), and moisture (z_q) are tuned to match the mean fluxes obtained in the direct numerical simulations. (2) The hydrostatic stability on the side walls is assumed to be neutral, as the buoyancy is parallel rather than normal to the side walls. More details on the wall modeling are addressed in Wang et al. (2024, see Section 2 and Appendix B therein).

The model setup is summarized in Table 1. The temperature of the bottom surface is set to be 300 K, the top surface to be 280 K, and the side walls to be 290 K. In previous SAM-Chamber simulations (Thomas et al., 2019; Yang et al., 2022, 2023), the side walls were set to be subsaturated such that the domain-averaged supersaturation without cloud is about 2.5% based on early chamber observations (Chandrakar et al., 2016). Subsaturated side walls serving as a sink for water vapor tend to evaporate droplets nearby. Sidewalls have been improved (i.e., closer to be water saturated) recently in the real Pi chamber, such that clouds can form at much smaller top and bottom temperature difference (Prabhakaran et al., 2020). In this study, all surfaces are set to be saturated with respect to water. The impact of side wall conditions on cloud properties will also be discussed. The simulation domain is 2 m × 2 m × 1 m with 6.25 cm grid spacing in all three directions. This grid spacing falls

Table 1. Summary of model setup.

Variable	Value
Bottom surface	$T_b = 300$ K, water saturated
Top surface	$T_t = 280$ K, water saturated
Side wall	$T_w = 290$ K, water saturated
Surface roughness	$z_0 = 0.75$ mm, $z_t = 0.619z_0$, $z_q = 0.756z_0$ (based on Wang et al., 2024)
Resolution	6.25 cm × 6.25 cm × 6.25 cm (32 × 32 × 16 grids)
Domain	2 m × 2 m × 1 m (height)
Aerosol property	Sodium chloride (NaCl), $r_a = 62.5$ nm
Cloud midrophysics scheme	CCN-based, Haze-capable (Yang et al., 2023)
Aerosol injection rate	$0.001 \sim 50$ cm^{-3}s^{-1} (detailed in the text)

in the inertial subrange, according to the direct numerical simulations with similar Reynolds number and Rayleigh number performed by Wang et al. (2023).

125   To mimic continuous injection of salt particles, monodisperse sodium chloride aerosol particles with a dry radius of 62.5 nm are added in each grid box after each time step, as in previous studies (Yang et al., 2022, 2023). Cloud droplet formation and growth by condensation are simulated using either CCN-based or haze-capable bin microphysics scheme. Both schemes are two-moment bin microphysics schemes based on Chen and Lamb (1994), with some differences detailed in Yang et al. (2023) and summarized below. For the CCN-based bin microphysics scheme (referred to as the CL$_{\text{CCN}}$), the droplet size distribution is

130   represented by 33 mass-doubling bins starting from 1 μm radius. Dry aerosol particles stay in the aerosol category and they will be moved to the first bin of the cloud category if the environmental supersaturation (in their grid box) is larger than the critical supersaturation of the aerosol (0.08% for a salt particle of 62.5 nm in radius). Solute and curvature effects are not considered for droplet growth by condensation. Note that such treatment of cloud microphysical processes – Twomey-type parameterization of droplet formation and neglect of solute and curvature effects on droplet growth – is quite common in atmospheric cloud

135   simulations. For the haze-capable bin microphysics scheme (referred to as the CL$_{\text{Haze}}$), aqueous droplets (including haze and cloud) are represented by 40 mass-doubling bins starting from 0.1 μm radius. Dry aerosol particles initially become haze with the equilibrium size at a relative humidity of 90% (same as in Yang et al., 2023). The growth of haze and cloud droplets via condensation is calculated explicitly with solute and curvature effects considered, and thus the activation process from haze particle to cloud droplet is naturally resolved. Following Yang et al. (2023), haze particles here refer to droplets smaller than

140   1 μm which is the bin edge closest to the critical radius of the aerosol (0.92 μm). Although all chamber surfaces are saturated with respect to water, droplet deactivation by evaporation can still occur due to turbulent supersaturation fluctuations. For the CL$_{\text{CCN}}$ scheme, evaporated droplets will be moved to the aerosol category if their radii get smaller than 1 μm in radius (the deactivation process). For the CL$_{\text{Haze}}$ scheme, deactivated droplets remain as haze particles. Efflorescence is not considered,

and if haze particles are less than 0.1 μm in radius, they stay in the smallest droplet bin. In both schemes, droplets can be lost
145   through the bottom surface due to sedimentation, but not through the side walls.

Following the modeling studies by Yang et al. (2023) and Wang et al. (2024), sodium chloride aerosol particles of a 62.5-nm radius are injected uniformly throughout the computational domain at a prescribed volumetric rate. A total of twenty-five aerosol injection rates (n_{in}) are employed to explore their impact on cloud properties. n_{in} ranges from 0.001 to 50 cm^{-3}s^{-1} in the following way: 0.001 to 0.005 cm^{-3}s^{-1} every 0.001 cm^{-3}s^{-1}, 0.01 to 0.05 cm^{-3}s^{-1} every 0.01 cm^{-3}s^{-1}, 0.1 to 0.5
150   cm^{-3}s^{-1} every 0.1 cm^{-3}s^{-1}, 1.0 to 5.0 cm^{-3}s^{-1} every 1.0 cm^{-3}s^{-1}, and 10.0 to 50.0 cm^{-3}s^{-1} every 10.0 cm^{-3}s^{-1}. Note that 14 values of n_{in} between 0.2 and 13 cm^{-3}s^{-1} were used in recent Pi chamber experiments (see Fig. 7 in Shaw et al., 2023), while only two values (0.25 and 2.5 cm^{-3}s^{-1}) were used in the Pi chamber simulations by Yang et al. (2023). Here, we cover a range of n_{in} that can be achieved in the Pi chamber, while extending n_{in} to represent extremely clean and polluted conditions. Although these exceptionally small and large n_{in} values might be difficult to achieve in the real chamber mainly
155   due to the current limitations of aerosol injection, they are helpful to explore haze-cloud interactions in various microphysics regimes that will be discussed in the next section.

The time step is 0.02 s and the total simulation is one hour. The domain-averaged data are output every minute from the beginning of the simulation, while instantaneous 3-D data are output every five minutes in the second half of the simulation.

3   Results

160   ### 3.1   Impact of aerosol injection rate on bulk cloud properties

Figure 1 shows the impact of n_{in} on supersaturation (s), droplet mean radius (r_d), N_d, and q_l. Here, q_l is the liquid water mixing ratio. Specifically, $q_l = q_c + q_h$ for the CL$_{\text{Haze}}$ scheme where q_c is cloud water mixing ratio (for droplets radii larger than 1 μm) and q_h is haze water mixing ratio (for droplets radii smaller than 1 μm), while $q_l = q_c$ for the CL$_{\text{CCN}}$ scheme. Each dot in the figure represents a temporally averaged (over the second half an hour) and spatially averaged (over the whole
165   domain) value for one aerosol injection rate when using either the CL$_{\text{CCN}}$ (black) or CL$_{\text{Haze}}$ (red) scheme. Results show that cloud microphysical properties based on these two schemes are similar, suggesting that using the Twomey-type activation parameterization is good enough to simulate the cloud, especially for s, N_d, and q_l.

The steady-state droplet size distributions based on the CL$_{\text{CCN}}$ and CL$_{\text{Haze}}$ schemes are shown in Fig. 2a-b. The distribution becomes narrower and shifts to smaller sizes with n_{in}, consistent with previous Pi chamber observations (Chandrakar et al.,
170   2016) and simulations (Thomas et al., 2019; Yang et al., 2023). The mode of small haze particles can only be captured by the CL$_{\text{Haze}}$ scheme, and is enhanced as n_{in} increases (Fig. 2b). We also compare the simulated size distributions with four analytical droplet size distributions: one with the formula $ar\exp(-br^4)$ (Fig. 2c), $ar\exp(-br^2)$ (Fig. 2d), $ar^2\exp(-br^3)$ (Fig. 2e), and $a\sqrt{r}\exp(-br^3)$ (Fig. 2f), where a and b represent the combinations of other variables and parameters except for r. All these analytical distributions use steady-state N_d and q_c from the SAM-Chamber simulations as input to calculate
175   the parameters a and b. The precise formulas are displayed in Fig. 2 c-f. Chandrakar et al. (2020) detailed the assumptions regarding these analytical distributions and evaluated them with the Pi chamber observations. In short, $ar\exp(-br^4)$ is de-
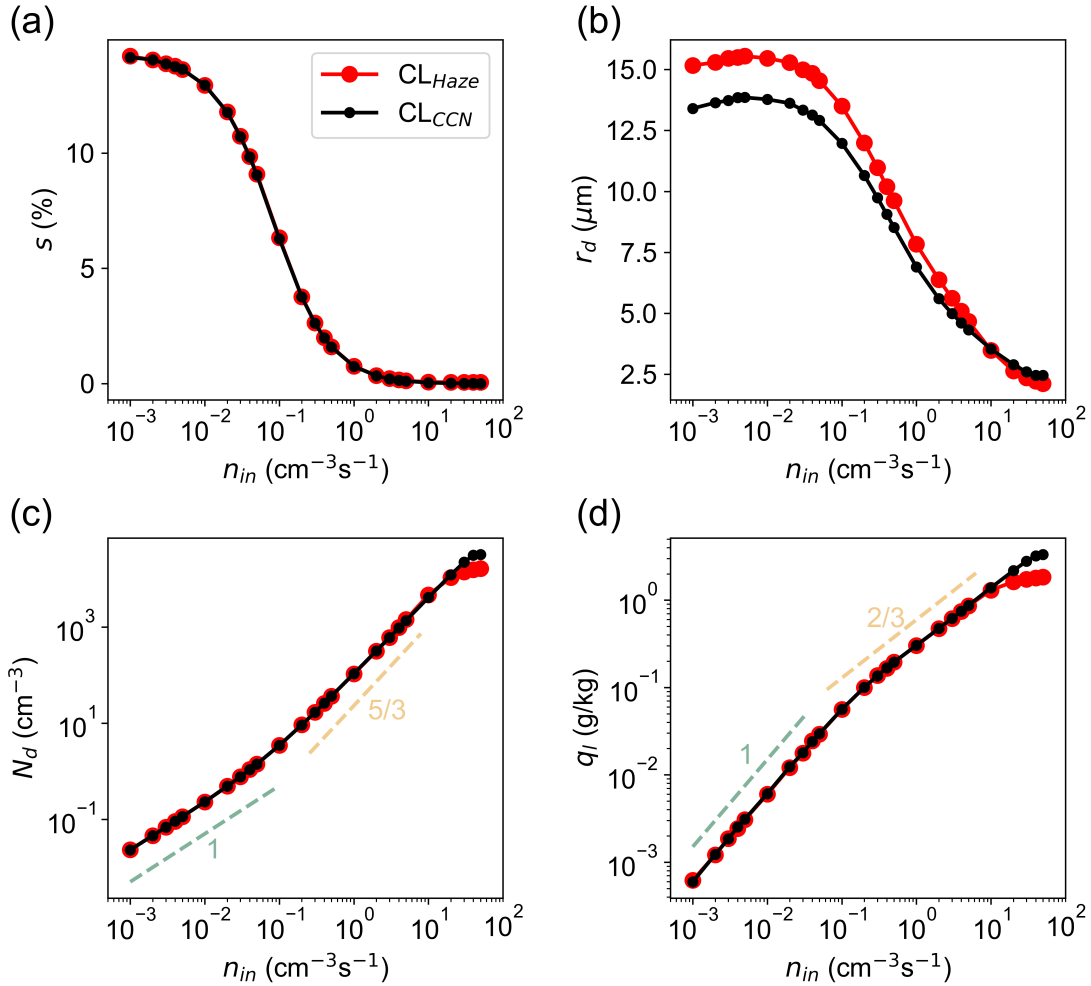
Figure 1. Spatial- (over the whole domain) and temporal-averaged (in the second half an hour) (a) supersaturation s, (b) mean droplet radius r_d, (c) droplet number concentration N_d, and (d) liquid water mixing ratio q_l at various aerosol injection rates. Black and red dots are results using CL_{CCN} and CL_{Haze} schemes, respectively. Each dot represents the average of the variable over the whole domain from the second half an hour. The light green and yellow colored dashed line in (c) and (d) are scaling relationship based on Shaw et al. (2023) in slow and fast microphysics regimes, respectively.

rived from the assumption of droplet growth in a constant supersaturation environment with size-dependent removal (Krueger, 2020), $ar \exp(-br^2)$ comes from droplet growth in a fluctuating supersaturation environment with size-independent removal (McGraw and Liu, 2006; Saito et al., 2019), $ar^2 \exp(-br^3)$ results from the principle of maximum entropy assumption (Liu and Hallett, 1998), and $a\sqrt{r} \exp(-br^3)$ comes from droplet growth in a fluctuating supersaturation environment with size-

dependent removal (Chandrakar et al., 2020). Results show that the simulated cloud droplet size distributions are closer to $ar\exp(-br^4)$, $ar^2\exp(-br^3)$, and $a\sqrt{r}\exp(-br^3)$, compared to $ar\exp(-br^2)$, which produces significantly broader spectra (Fig. 2d). Furthermore, the haze mode is not captured by any analytical distribution, simply because none of those analytical models considers the full activation process – from haze particles to cloud droplets.
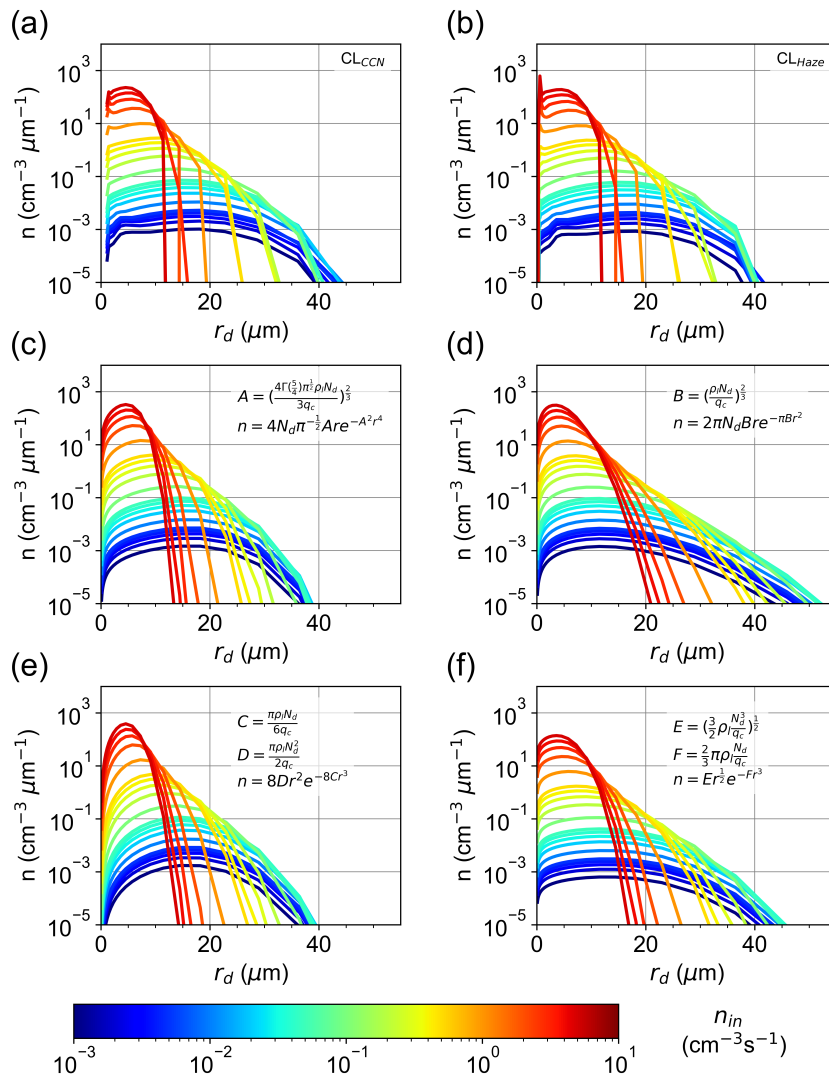
Figure 2. Steady-sate droplet size distributions for different aerosol injection rates when using (a) CL_{CCN} and (b) CL_{Haze} schemes. (c-f) Four analytical droplet size distributions using the domain-averaged N_d and q_c as input, with the precise formulas displayed in the legend.

The slow microphysics regime is observed when $n_{in} < 0.1\,\mathrm{cm^{-3}s^{-1}}$. In this regime, few droplets (i.e., very small N_d shown in Fig. 1c) grow in a high supersaturated environment (Fig. 1a) before they fall out, leading to a roughly constant r_d (Fig. 1b)

Table 2. Spatial and temporal averaged aerosol/haze number concentration (N_a/N_h, cm^{-3}), cloud droplet number concentration (N_d, cm^{-3}), mean cloud droplet radius (r_d, μm), droplet activation rate (R_{act}, cm^{-3}s^{-1}), and droplet deactivation rate (R_{deact}, cm^{-3}s^{-1}) at different aerosol injection rates (n_{in}, cm^{-3}s^{-1}). Values before and after the slash are results when using the CL$_{\text{CCN}}$ and CL$_{\text{Haze}}$ schemes, respectively. Each value is averaged over the whole domain in the second half an hour at a given n_{in}.

n_{in}	N_a/N_h	N_d	r_d	R_{act}	R_{deact}
0.001	0 / 1.0×10^{-4}	0.023 / 0.023	13 / 15	0.001 / 0.001	0 / 0
0.002	0 / 2.1×10^{-4}	0.046 / 0.046	14 / 15	0.002 / 0.002	0 / 0
0.003	0 / 3.2×10^{-4}	0.068 / 0.069	14 / 15	0.003 / 0.003	0 / 0
0.004	0 / 4.3×10^{-4}	0.092 / 0.091	14 / 15	0.004 / 0.004	0 / 0
0.005	0 / 5.5×10^{-4}	0.11 / 0.11	14 / 16	0.005 / 0.005	0 / 0
0.01	0 / 0.0012	0.23 / 0.23	14 / 15	0.01 / 0.01	0 / 0
0.02	0 / 0.0026	0.49 / 0.49	14 / 15	0.02 / 0.02	0 / 0
0.03	0 / 0.0043	0.77 / 0.77	13 / 15	0.03 / 0.03	0 / 0
0.04	0 / 0.0063	1.1 / 1.1	13 / 15	0.04 / 0.04	0 / 0
0.05	0 / 0.0086	1.4 / 1.4	13 / 15	0.05 / 0.05	0 / 0
0.1	0 / 0.026	3.5 / 3.5	12 / 13	0.1 / 0.1	0 / 8.8×10^{-20}
0.2	4.3×10^{-7} / 0.095	9.2 / 9.2	11 / 12	0.2 / 0.2	0 / 2.5×10^{-7}
0.3	7.4×10^{-5} / 0.25	17 / 17	9.7 / 11	0.3 / 0.3	8.4×10^{-5} / 3.4×10^{-5}
0.4	8.8×10^{-4} / 0.53	26 / 26	9.1 / 10	0.4 / 0.4	0.0012 / 3.0×10^{-4}
0.5	0.0038 / 0.96	37 / 37	8.5 / 9.6	0.51 / 0.51	0.0048 / 0.0014
1	0.19 / 5.5	108 / 107	6.9 / 7.8	1.2 / 1	0.18 / 0.032
2	4.8 / 30	321 / 316	5.6 / 6.4	3.8 / 2.3	1.8 / 0.24
3	19 / 73	608 / 607	5 / 5.6	7 / 3.5	4.1 / 0.52
4	39 / 127	955 / 978	4.6 / 5.1	10 / 4.9	6.3 / 0.96
5	65 / 198	1.4×10^3 / 1.4×10^3	4.3 / 4.7	13 / 7.1	8.2 / 2

and a linear relationship between n_{in} and N_d (Fig. 1c) and q_l (Fig. 1d) as predicted by Shaw et al. (2023). When 0.1 cm^{-3}s^{-1} $< n_{in} <$ 10.0 cm^{-3}s^{-1}, the cloud is in the fast microphysics regime, in which more cloud droplets compete with each other for available water vapor needed for their condensational growth, leading to larger N_d and smaller r_d. In this regime, s and r_d decrease with n_{in}, while $N_d \sim n_{in}^{5/3}$ and $q_l \sim n_{in}^{2/3}$, consistent with theory. However, it is interesting to note that the scaling laws for N_d and q_l do not work well for $n_{in} \geq 10.0$ cm^{-3}s^{-1} when using the CL$_{\text{Haze}}$ scheme. This regime turns out to be very important for haze-cloud interactions that will be explored in the following section.

Table 2 summarizes the spatially and temporally averaged cloud microphysical properties for $n_{in} \leq 5.0$ cm^{-3}s^{-1} when the scaling laws work reasonably well. Those variables include aerosol (when using the CL$_{\text{CCN}}$ scheme) / haze (when using the CL$_{\text{Haze}}$ scheme) number concentration (N_a/N_h), cloud droplet number concentration (N_d), mean cloud droplet radius

(r_d), droplet activation rate (R_{act}), and deactivation rate (R_{deact}). The droplet activation rate represents the number of newly formed cloud droplets per cubic centimeter per second, while the deactivation rate represents the reverse process. Note that the net activation rate $(R_{act} - R_{deact})$ is close to n_{in} for each case suggesting that the cloud reaches a quasi-steady state. It is worth mentioning that although the simulated cloud properties using the two schemes are similar, unactivated particle concentration

200 $(N_a$ or $N_h)$, R_{act}, and R_{deact} are quite different for $n_{in} \geq 1.0$ cm^{-3}s^{-1}. Our results suggest that haze-cloud interactions are important in the fast microphysics regime. In fact, the transition from the slow to the fast microphysics regime occurs when haze particles become important: $N_h/N_d > 5\%$ and $R_{deact}/R_{act} > 3\%$ for $n_{in} \geq 1.0$ cm^{-3}s^{-1} (Fig. 3).
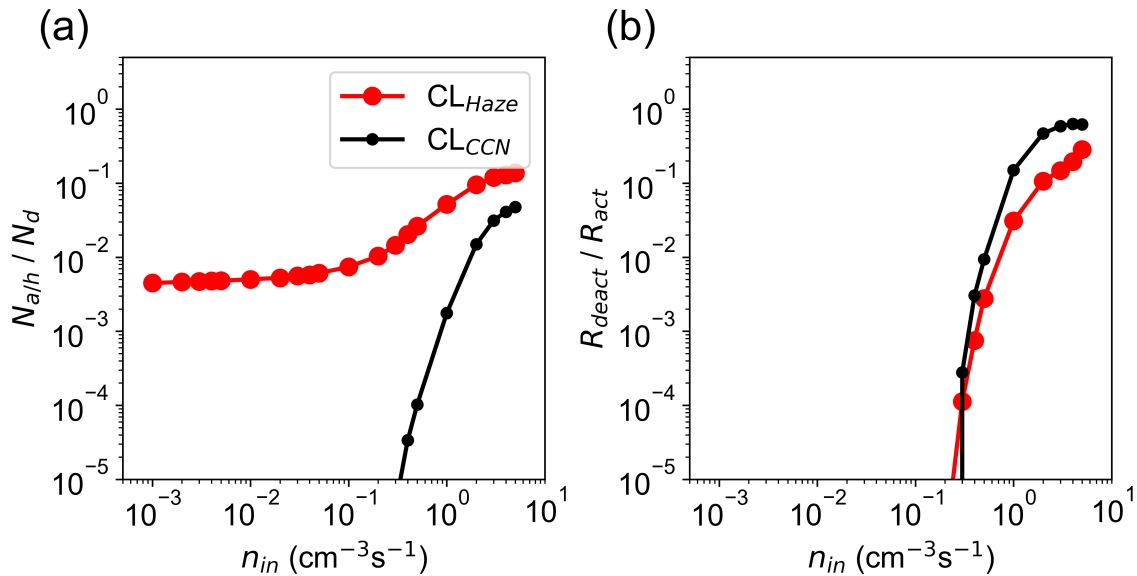
Figure 3. (a) The ratio of the unactivated particle number concentration to the cloud droplet number concentration for different aerosol injection rates (n_{in}). Unactivated particles are aerosol particles when using the CL$_{CCN}$ scheme, or haze particles when using the CL$_{Haze}$ scheme. (b) Ratio of deactivation to activation rate for different n_{in}.

Shaw et al. (2023) predicted that the transition from slow to fast microphysics regimes occurs at Da ≈ 1. Here Da is the Damköhler number, defined as the ratio of turbulent mixing time (τ_m) to phase relaxation time (τ_p) (see Eq. 1 in Lehmann

205 et al., 2009). τ_p is inversely proportional to the product of N_d and r_d, which can be determined from our simulation results. Take $n_{in} = 0.1$ cm^{-3}s^{-1} as an example, $\tau_p \approx 70$ s, calculated from $N_d = 3.5$ cm^{-3} and $r_d = 12$ μm based on Table 2 (using Eq. 18 in Korolev and Mazin, 2003). The apparent transition between slow and fast regimes as shown in Fig. 1 provides an opportunity to estimate τ_m, which is on the order of 100 s for our boundary conditions (e.g., 20 K difference in top and bottom temperature).

3.2 Haze-cloud interactions in the polluted conditions

Figure 1 c and d show that N_d and q_l do not follow the aforementioned scaling laws for $n_{in} \geq 10\,\mathrm{cm^{-3}s^{-1}}$. In this section, we explore the reason for this departure and show that haze-cloud interaction in these extremely polluted conditions can lead to some new microphysics regimes, including cloud oscillation, cloud collapse, and haze only.

3.2.1 Cloud oscillation

One possible reason for the observed departure for N_d and q_l in the polluted conditions ($n_{in} \geq 10\,\mathrm{cm^{-3}s^{-1}}$) is that the cloud does not reach a steady state after one hour. To rule out this possibility, we extend the simulations of the largest five n_{in} (10, 20, 30, 40, 50 $\mathrm{cm^{-3}s^{-1}}$) to a total simulation time of ten hours. Figure 4 shows the time series of domain-averaged q_l, q_c, N_d, N_a (for the CL$_{\mathrm{CCN}}$ scheme), N_h (for the CL$_{\mathrm{Haze}}$ scheme), and r_d. Note that $q_l \geq q_c$ when using the CL$_{\mathrm{Haze}}$ scheme, and the difference ($q_l - q_c$) is haze water mixing ratio (q_h), while $q_l = q_c$ when using the CL$_{\mathrm{CCN}}$ scheme. Results show that q_l, N_d, and r_d always reach a steady state when using the CL$_{\mathrm{CCN}}$ scheme. Note that N_a increases with time for $n_{in} \geq 10\,\mathrm{cm^{-3}s^{-1}}$. This is because the sink of aerosol due to droplet activation is smaller than the source of aerosol due to aerosol injection, and thus aerosol particles accumulate. When using the CL$_{\mathrm{Haze}}$ scheme, the cloud reaches a steady state for an aerosol injection rate of 10 $\mathrm{cm^{-3}s^{-1}}$, where q_l is dominated by q_c. In contrast, when n_{in} is 20 $\mathrm{cm^{-3}s^{-1}}$ or higher, cloud microphysical properties (such as q_l, q_c, N_d, r_d) oscillate. The oscillation period increases as n_{in} increases, and the periods are 15, 20, 25, and 30 min for $n_{in} = 20, 30, 40$, and $50\,\mathrm{cm^{-3}s^{-1}}$. N_h also oscillates as N_d but in the opposite way: the local maximum of N_d corresponds to the local minimum of N_h, suggesting the burst of droplet formation is due to the activation of a large number of haze particles. The ratio of q_h (i.e., q_l-q_c) to q_l increases with n_{in} and it can be up to 30% for $n_{in} = 50\,\mathrm{cm^{-3}s^{-1}}$. Note that the oscillation of the mean r_d is mainly due to droplet activation/deactivation, not due to the physical growth/evaporation of cloud droplets. For example, the rapid formation of numerous small cloud droplets decreases the mean r_d accordingly.

Figure 5 shows the time evolution of mean profiles of cloud properties in the last hour of the simulation for $n_{in} = 40$ $\mathrm{cm^{-3}s^{-1}}$. We note that q_c and q_h oscillate out of phase (Fig. 5 a vs. d), while q_l is mainly influenced by q_c (Fig. 5 g). Larger q_c (q_h) corresponds to smaller N_d (N_h), and vice versa (Fig. 5 a vs. b and d vs. e). The anti-correlation between q_c and N_d is opposite to their scaling relationships in the slow and fast microphysics, which are $q_c \sim N_d$ and $q_c \sim N_d^{2/5}$, respectively (Shaw et al., 2023). The sharp increase in N_d (Fig. 5b) corresponds to a larger activation rate (Fig. 5c) due to the enhanced supersaturation (Fig. 5i), while the decrease in N_d corresponds to a larger deactivation rate and a smaller supersaturation.

To further explore the mechanism of the oscillation, we pick one oscillation cycle for $n_{in} = 40\,\mathrm{cm^{-3}s^{-1}}$. Figure 6 shows the phase diagram of four pairs of variables: N_h vs. N_d, q_h vs. q_c, q_h vs. N_h, and q_c vs. N_d. Each circle in the figure represents the domain-averaged value at one time and its color represents the domain-averaged supersaturation with the unit of ‰₀, one per ten thousand. The size of the circle represents the mean droplet radius in a relative way: a larger circle means a larger r_d. The oscillation behavior can be explained by the circulation in the phase diagram. Taking Fig. 6d as an example: Start from the lower left corner where q_c and N_d are low, s is high, and r_d is large. When $s > s_{crit}$ ($s_{crit} \approx 8\,\text{‰₀}$ in this study), a huge amount of droplets are activated leading to a sharp increase in N_d. Newly formed cloud droplets significantly decrease the
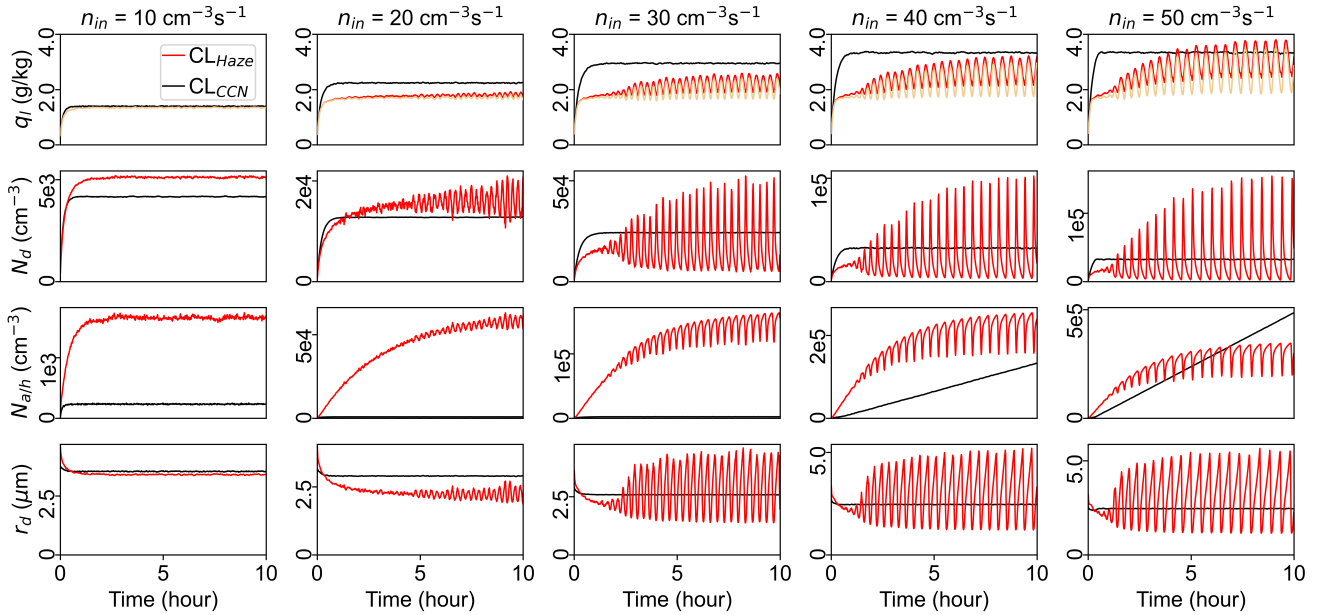
Figure 4. Time series of domain-averaged q_l (first row), N_d (second row), N_a/N_h (third row), and r_d (forth row) for five different n_{in}: 10, 20, 30, 40, and 50 cm^{-3}s^{-1}. The yellow line in the first row represents the cloud water mixing ratio (q_c) when using the CL$_{\text{Haze}}$ scheme.

mean r_d and they grow in slightly supersaturated conditions, leading to an increase in q_l and a decrease in s. Shortly thereafter, N_d decreases because droplet activation is suppressed when $s < s_{crit}$, and meanwhile, droplets are lost due to sedimentation

245 and deactivation. Droplet deactivation causes a recovery of N_h and an increase in q_h (Fig. 6 a,b). The decrease in N_d finally results in a decrease in q_l and an increase in s. When $s > s_{crit}$, another period starts. Note that droplet activation leads to an increase in N_d and a decrease in N_h simultaneously, thus causing the perfect anticorrelation between N_h and N_d (Fig. 6a). In contrast, mass and number concentrations (either q_h vs. N_h or q_c vs. N_d) peak at different times, because it takes time for droplet/haze to grow. It is interesting to see that the oscillation evolves with time clockwise in $q_h - N_h$ diagram (Fig. 6c) and

250 anticlockwise in $q_c - N_d$ diagram (Fig. 6d), suggesting that q_h is ahead of N_h while N_d is ahead of q_c in their phases, analogous to a predator-prey dynamical system.

3.2.2 Cloud oscillation in a box model

To make sure the oscillation is physical and not due to numerical artifact from using an Eulerian-based bin microphysics scheme, we develop a box model using a particle-based microphysics approach to simulate cloud in a convection chamber. The

255 particle-based treatment, analogous to Lagrangian droplet method, directly calculates and tracks the time evolution of droplet size. The well-mixed cloud system can be described by a set of differential equations detailed below.
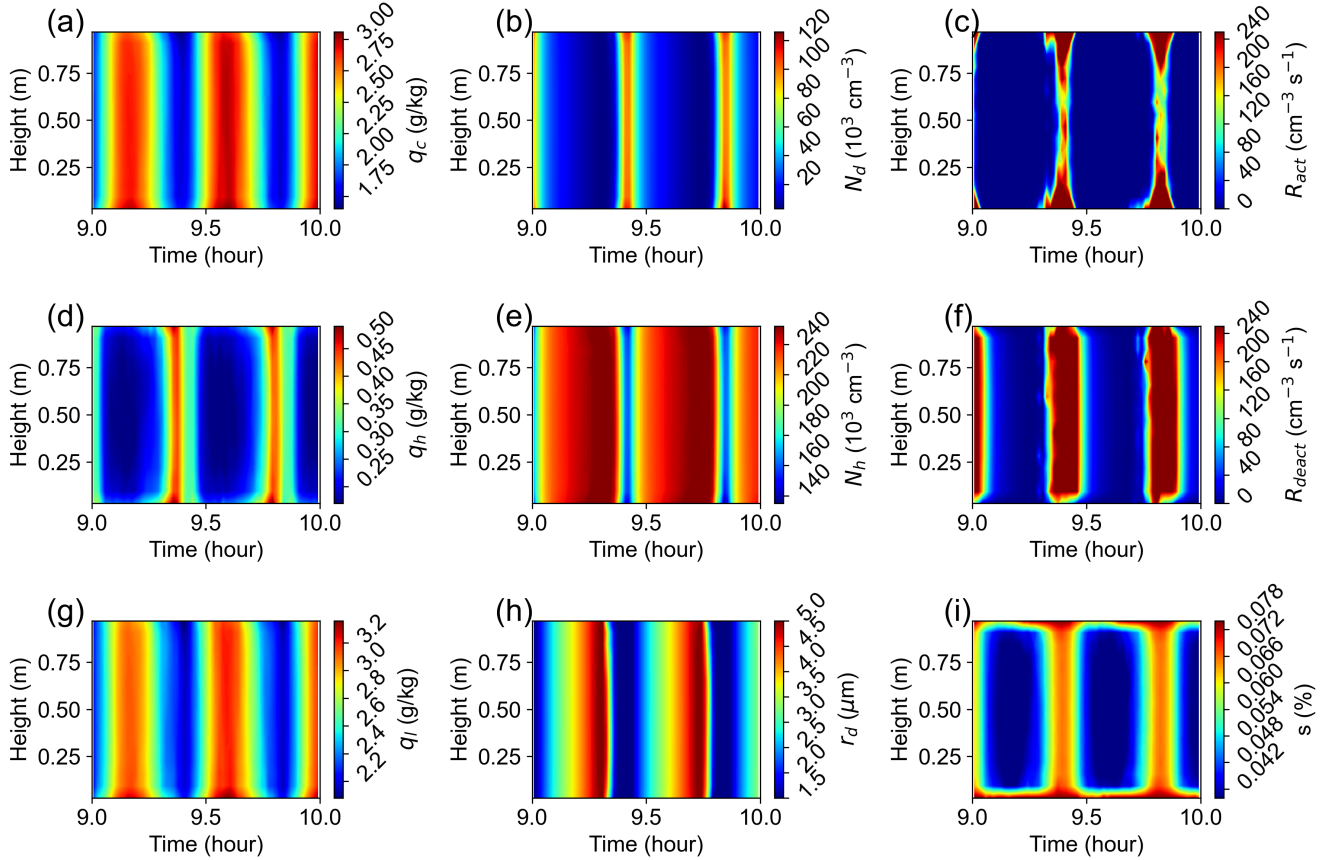
Figure 5. Time evolution of mean profiles of (a) cloud water mixing ratio, q_c, (b) cloud droplet number concentration, N_d, (c) activation rate, R_{act}, (d) haze water mixing ratio, q_h, (e) haze number concentration, N_h, (f) deactivation rate, R_{deact}, (g) total water mixing ratio, q_l, (h) droplet radius r_d, and (i) supersaturation, s, for $n_{in} = 40\ \text{cm}^{-3}\text{s}^{-1}$ between 9 and 10 hours when using the CL$_{\text{Haze}}$ scheme. It is the the last simulation hour of Fig. 4, second column.

Following by Shaw et al. (2023), the time derivative of mean air temperature can be expressed as

$$\frac{dT}{dt} = \frac{T_0 - T}{\tau_m} + \frac{L}{c_p}\frac{dq_l}{dt}, \tag{1}$$

where T_0 is the reference temperature, which equals to the mean temperature in the chamber without cloud droplets. L is the
260 latent heat of vaporization of water and c_p is the specific heat of air. τ_m is the mixing time scale, which quantifies how efficient T can be restored to T_0. Similarly, the time derivative of water vapor mixing ratio is expressed as

$$\frac{dq_v}{dt} = \frac{q_{v0} - q_v}{\tau_m} - \frac{dq_l}{dt}, \tag{2}$$
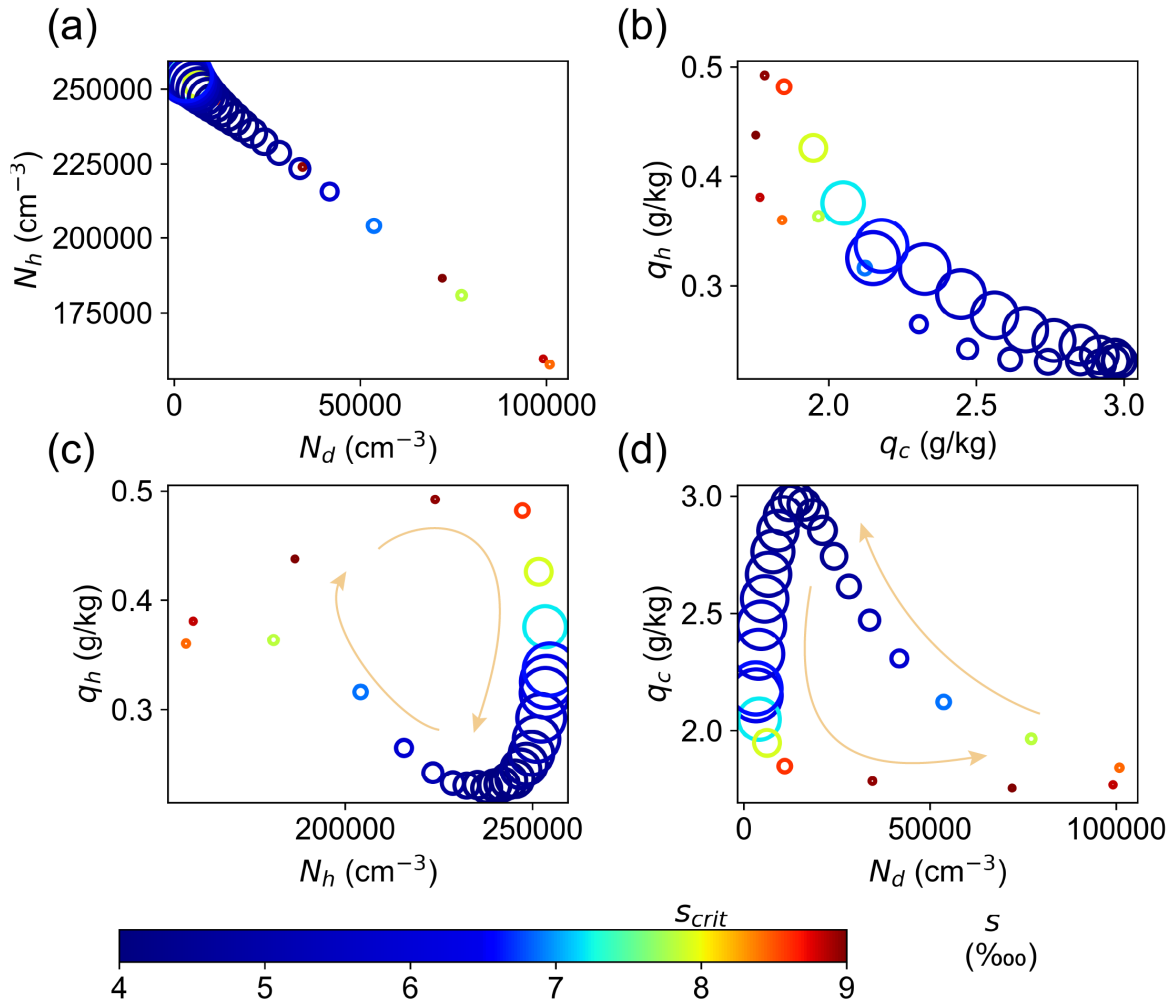
Figure 6. The relationship between domain-averaged (a) N_h vs. N_d, (b) q_h vs. q_c, (c) q_h vs. N_h, and (d) q_c vs. N_d over one cycle of cloud oscillation at $n_{in} = 40 \, \mathrm{cm}^{-3}\mathrm{s}^{-1}$. The size of the circle represents the mean droplet radius in a relative way, e.g., a larger circle means a larger r_d. Its color stands for the domain-averaged supersaturation with the unit of ‰₀, one per ten thousand. The arrows in (c) and (d) represents its time evolution in one cycle.

where q_{v0} is the reference water vapor mixing ratio, which equals to the mean water vapor mixing ratio in a cloud-free condition assuming both top and bottom surfaces are saturated with respect to water. The last terms in Eqs. 1 and 2 represent the impact
265 of droplet condensational growth (dq_l/dt) on T and q_v, respectively.

To be consistent with the model setup of large-eddy simulations, monodisperse dry aerosol particles with radii of 62.5 nm are added at a constant rate using a particle-based super droplet method. Specifically, one new super particle (hereafter referred to as particle) is added at a constant rate: every second for $n_{in} \leq 5 \, \mathrm{cm}^{-3}\mathrm{s}^{-1}$ or every 20 seconds for the largest five n_{in} to save computational time. Each particle represents numerous real particles per unit volume. We refer to this as multiplicity, denoted hereafter as n_i, which represents the concentration of a particle with an index of i. The growth rate of droplet radius with an index of i is given by,

$$\frac{dr_i}{dt} = \frac{G}{r_i}\left(s - \frac{A}{r_i} + \frac{B}{r_i^3}\right), \tag{3}$$

where G is the growth factor and s is the supersaturation depending on both T and q_v. A/r_i and B/r_i^3 are curvature and solute effects, respectively, in which A and B are constant for given thermodynamic and aerosol conditions (Eq. 6.6 in Yau and Rogers, 1996). The change of liquid water mixing ratio, which is linked to the last terms in Eqs. 1 and 2, can be calculated as the sum of mass change of all droplets,

$$\frac{dq_l}{dt} = \frac{4\pi\rho_l G}{\rho_a}\sum_i n_i r_i^2 \frac{dr_i}{dt}. \tag{4}$$

Here ρ_a and ρ_l are air and liquid water densities, respectively.

Equations 1-4 are the governing equations to describe the bulk properties of a well-mixed cloud in a convection chamber. We use an ordinary differential equation solver to solve the above set of nonlinear and stiff equations (Brown et al., 1989). The total number of equations in the system depends on the number of particles. For example, if we have 100 particles at a given moment, the total number of equations to be solved is 102 (100 for r_i, one for T, and one for q_v). The same solver has been used in adiabatic cloud parcel models to properly calculate the growth of haze particles and the droplet activation process in the real atmosphere (Xue and Feingold, 2004; Chen et al., 2016; Yang et al., 2016).

Without sedimentation, the number of particles in the system would increase with time due to continuous injection, which eventually makes the system numerically unsolvable. In reality, the number of particles increase with time at the beginning, but it could reach a steady state if the rate of increase of particles due to injection is balanced by its loss rate due to sedimentation. To represent the impact of gravitational sedimentation, n_i decreases with time as

$$\delta n_i = n_i \exp\left[-\frac{\delta t}{\tau_{sed}(r_i)}\right], \tag{5}$$

where δt is set to be one second and δn_i is the decreased amount of multiplicity of a particle with the index of i. τ_{sed} is the characteristic sedimentation time of a droplet with a radius of r_i in a convection cloud chamber,

$$\tau_{sed}(r_i) = \frac{H}{v_t(r_i)}. \tag{6}$$

Here H is the chamber height of 1 m and v_t is the terminal velocity of a droplet with a radius of r_i. If n_i is smaller than a threshold of $10^{-10} \, \mathrm{cm}^{-3}$, we remove that particle.

We conduct a total of 25 cases with the same forcing (i.e., T_0, q_{v0}, and τ_m) but different n_{in}, which are the same as those used in previous large-eddy simulations. For a given n_{in}, the multiplicity of a newly added particle (n_{i0}) and the injection

frequency are determined such that their product equals n_{in}. For example, injection of a particle with $n_{i0} = 0.5$ cm^{-3} every second corresponds to $n_{in} = 0.5$ cm^{-3}s^{-1}, while injection of a particle with $n_{i0} = 200$ cm^{-3} every 20 seconds corresponds to $n_{in} = 10$ cm^{-3}s^{-1}. T_0 and q_{v0} are set to be 290 K and 13.9 g kg^{-1}, which are consistent with the cloud-free humid condition

300 in a convection chamber with a top temperature of 280 K, a bottom temperature of 300 K, and both surfaces are saturated with respect to water. τ_m is set to be 165 s, such that the steady-state s from the box model (Fig. 7a) agrees with that from LES (Fig. 1a). Note that the value of τ_m used here is not exactly the same as the estimated τ_m for $Da = 1$ based on LES results above, but they are the same order of magnitude. One possible reason for this difference is the uncertainty to estimate where fast-slow transition occurs.

305 Results show that the impact of n_{in} on cloud properties based on the box model are consistent with those from LES (compare Fig. 7 vs. Fig. 1). Slow and fast microphysics regimes are also captured by the box model (Fig. 7c,d). It is encouraging to see that the transition between slow and fast microphysics regimes occurs at around n_{in} of 0.1 cm^{-3}s^{-1}, which agrees well with LES. The box model also captures cloud oscillation for the largest five n_{in} (10, 20, 30, 40, 50 cm^{-3}s^{-1}), as shown in Fig. 8. The oscillation frequency decreases with the increase of n_{in}, which is consistent with LES results (Fig. 4). Note that, for cloud

310 oscillation cases, s, r_d, N_d, and q_l in Fig. 7 are averaged over one cycle and it is interesting to see that N_d vs. n_{in} and q_l vs. n_{in} agree better with the aforementioned scaling laws in the fast microphysics regime, compared with LES (compare Fig. 7 c,d vs. Fig. 1 c,d). This might be due to the bias in representing droplet distribution when using limited number of discretized bins in polluted conditions, or the systematic difference between a 3-D LES and a box model.

Our results indicate that the box model can represent the mean bulk cloud properties in a convection chamber. Cloud oscil-

315 lation at large n_{in} is therefore physically plausible, mainly due to haze-cloud interactions in polluted conditions (i.e. when s is close to s_{crit}). In contrast, simulations using the CL$_{CCN}$ scheme do not show oscillations (black lines in Fig. 4). Our results suggest that, to properly simulate haze-cloud interactions in highly polluted clouds, we need to fully resolve the activation process instead of using the Twomey-type parameterization.

3.2.3 Cloud collapse

320 For the simulations above, the side walls are set to be saturated with respect to water. In reality, the side walls in the Pi chamber could be subsaturated, which could enhance droplet deactivation. To investigate the impact of side wall humidity (RH$_{wall}$) on cloud oscillation, we set RH$_{wall}$ to be 90, 70, 50, and 30% for $n_{in} = 20$ cm^{-3}s^{-1}. This is similar to the entrainment of subsaturated air into a natural cloud. Results show that q_l decreases as RH$_{wall}$ decreases (Fig. 9 first row). This is because subsaturated side walls serve as a water sink to evaporate droplets and thus enhance haze-cloud interactions. Note that q_h can

325 be as large as q_c (e.g., for RH$_{wall}$ of 30% in the end of the simulation), which cannot be captured when using the CL$_{CCN}$ scheme. The cloud always reaches a steady state when using the CL$_{CCN}$ scheme. In contrast, when using the CL$_{Haze}$ scheme, the cloud oscillates for RH$_{wall}$ of 90 and 70%, but it can reach a steady state for RH$_{wall}$ of 50%, and more interestingly, it tends to collapse for RH$_{wall}$ of 30% (Fig. 9 second row). Here we refer the "cloud collapse" as the observed significant decrease in N_d at low RH$_{wall}$ conditions. Note that the cloud does not dissipate because q_c still reaches a steady state.
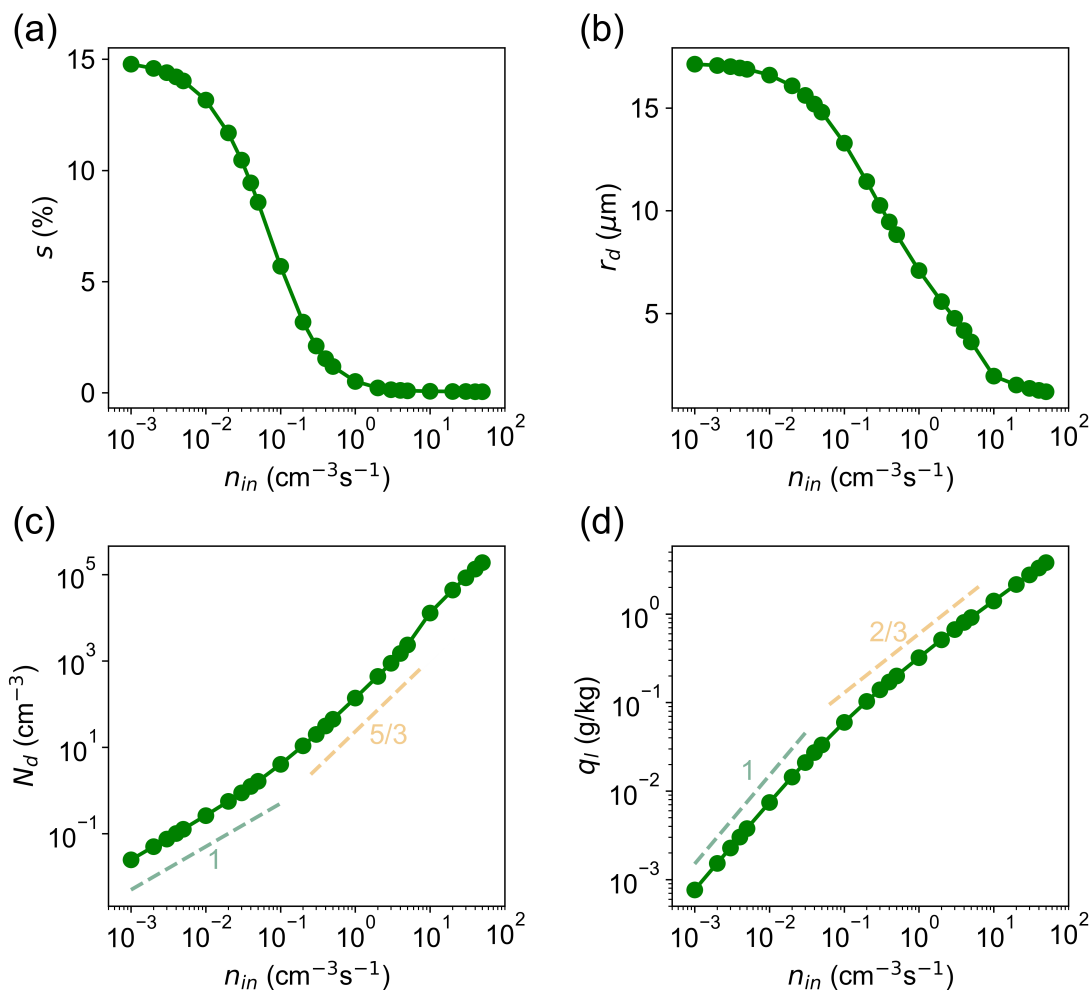
Figure 7. Impact of n_{in} on (a) supersaturation s, (b) mean droplet radius r_d, (c) droplet number concentration N_d, and (d) liquid water mixing ratio q_l based on a box model using a particle-based microphysics approach. The cloud oscillates for the largest five n_{in} (10, 20, 30, 40, 50 cm^{-3}s^{-1}), as shown in Fig. 8. For those cases, s, r_d, N_d, and q_l are averaged over one cycle. The light green and yellow colored dashed line in (c) and (d) are scaling relationship based on Shaw et al. (2023) for slow and fast regimes, respectively.

330   Our results suggest that cloud oscillation and cloud collapse result from haze-cloud interactions in a homogeneous and inhomogeneous supersaturation field, respectively. When the side walls are close to be saturated, the supersaturation field is almost homogeneous everywhere in the chamber except very close to the top and bottom surfaces. Such a homogeneous supersaturation field allows synchronized droplet activation or deactivation to occur throughout the entire chamber and thus leads to cloud oscillation as explained above and Fig. 6. However, when the side walls are considerably drier, the supersaturation
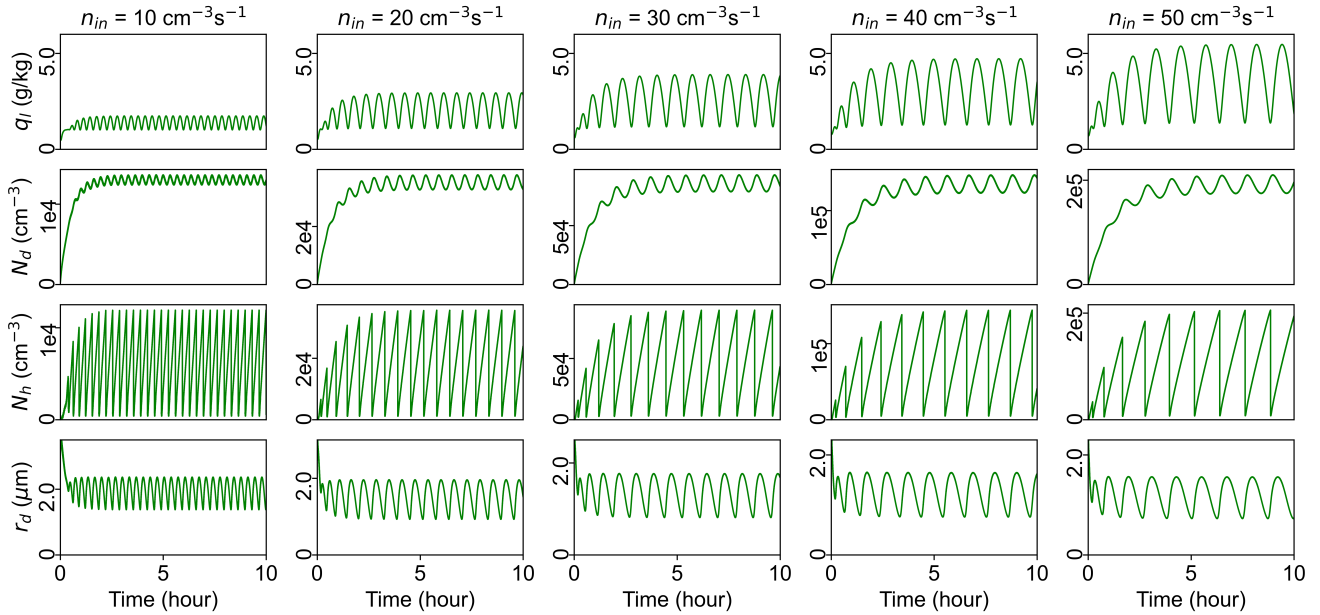
Figure 8. Similar to Fig. 4, time series of q_l (first row), N_d (second row), N_h (third row), and r_d from a box model using a Lagrangian microphysics approach for the five largest n_{in}: 10, 20, 30, 40, 50 cm^{-3}s^{-1}.

field in the chamber is not homogeneous: air close to the side wall is subsaturated while air close to the center, top and bottom surfaces is supersaturated. Such an inhomogeneous field causes droplet activation in one region and deactivation in another region. For a moderate dry side wall (i.e., RH$_{\text{wall}}$ of 50%), a steady state might be reached if the net activation rate is balanced by the droplet sedimentation rate. For an extremely dry side wall (i.e., RH$_{\text{wall}}$ of 30%), the chamber can be considered as a machine to efficiently transfer cloud droplets to haze particles over time, leading to the cloud collapse.

3.2.4 Haze-only regime

So far, our results show that beside slow and fast microphysics regimes, there exists a cloud oscillation regime at high aerosol injection rate due to haze-cloud interactions. In the oscillation regime, the oscillation frequency decreases and the haze number concentration increases as n_{in} increases. It raises a question of what would happen if n_{in} is extremely large? Would there be another regime in which there are only haze particles and no cloud droplets (i.e., the oscillation frequency approaches zero)? Here, we develop a simple model to investigate the properties of a postulated haze-only regime.

Let us assume only haze particles exist in the chamber at an extremely high aerosol injection rate. Following the approach of Shaw et al. (2023) (Eqs. 56 and 57 therein), in the steady state, the mean air temperature would be higher than the reference temperature (i.e., T_0, same as in our Eq. 1) due to latent heat release from the formation of haze particles,

$$T = T_0 + \tau_m \frac{L}{c_p} \frac{dq_l}{dt}. \tag{7}$$
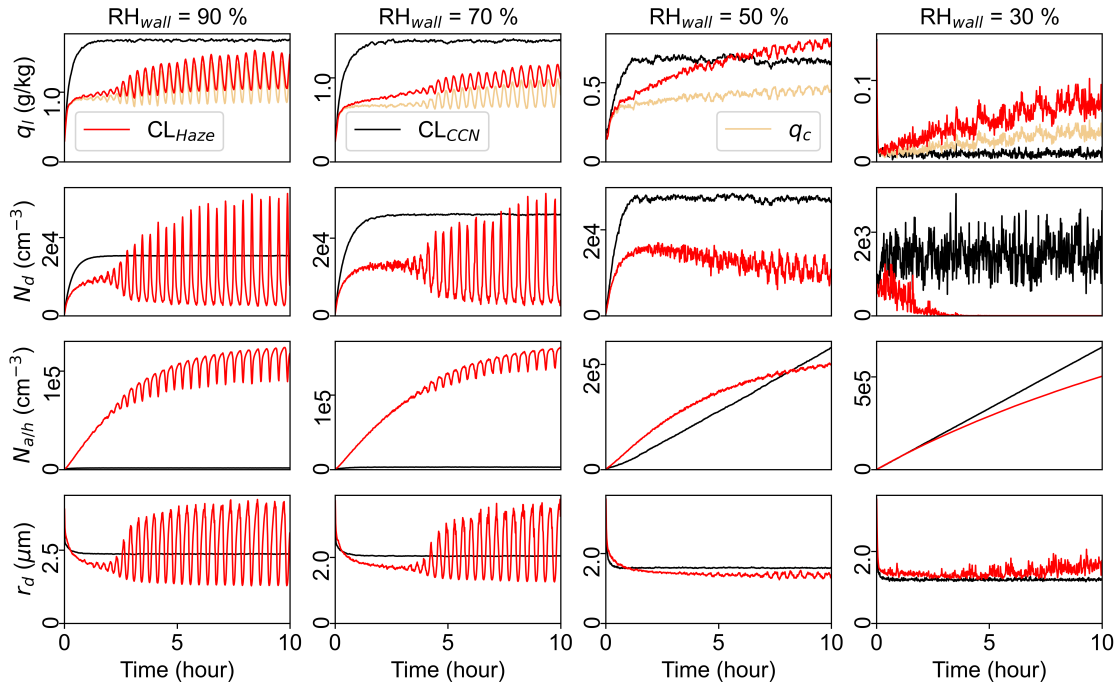
Figure 9. Time series of domain-averaged q_l (first row), N_d (second row), N_a/N_h (third row), and r_d (fourth row) at a n_{in} of 20 cm^{-3}s^{-1} with four different size wall relative humidity, RH$_{wall}$ = 90, 70, 50, and 30%.

350 Similarly, q_v would be smaller than the reference water vapor mixing ratio (i.e., q_{v0}, same as in our Eq. 2) due to water uptake by haze particles,

$$q_v = q_{v0} - \tau_m \frac{dq_l}{dt}. \tag{8}$$

In the haze-only regime, condensation is dominated by the formation of haze particles,

$$\frac{dq_l}{dt} = \frac{4}{3}\pi \rho_l r_{eq}^3 n_{in}. \tag{9}$$

355 Here r_{eq} is the equilibrium haze particle radius at a given $s < s_{crit}$. We rely on the fact that dry aerosol particles become haze particles through deliquescence and reach their equilibrium size within a very short time. r_{eq} depends on aerosol properties and the environmental relative humidity (RH=1+s), and it can be expressed as a function of RH close to but smaller than 100%, based on Lewis (2019),

$$r_{eq} = r_{dry} \left(\frac{1}{1 - RH} \right)^{1/3}, \tag{10}$$

360   where r_{dry} is the radius of dry aerosol. A similar expression of r_{eq} is also derived by Khvorostyanov and Curry (2007) (Eq. 16 therein).

    Meanwhile, a steady-state haze-only system requires that the formation of haze particles through injection is balanced by their loss due to sedimentation,

$$\frac{dq_l}{dt} = \frac{q_l}{\tau_{sed}}. \tag{11}$$

365   Here $q_l = q_h$ and τ_{sed} is the characteristic sedimentation time of haze particles with a radius of r_{eq} (see Eq. 6).
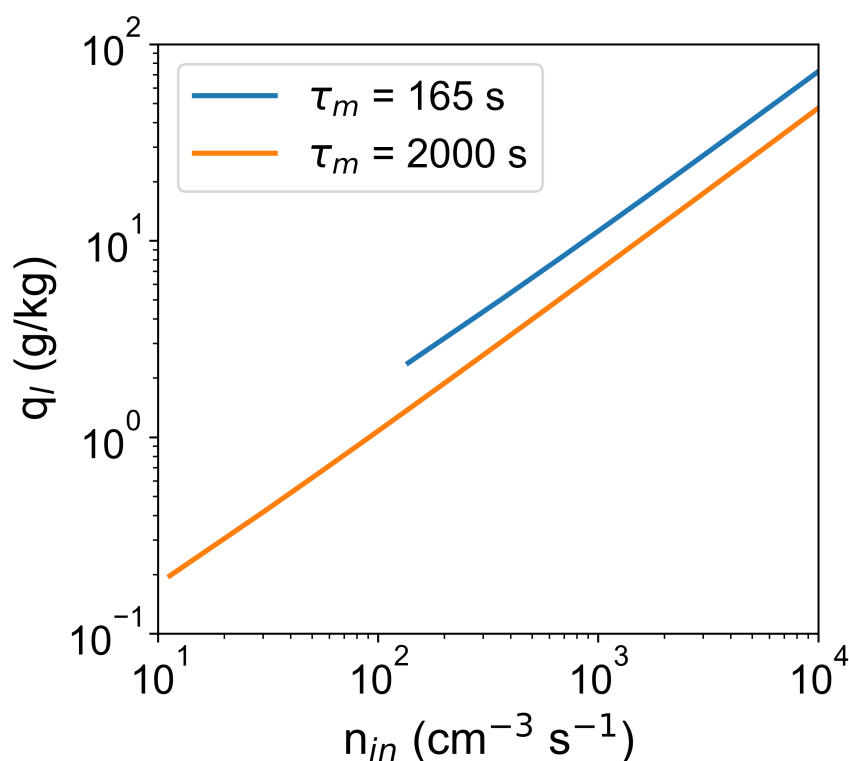
Figure 10. Change of equilibrium liquid water mixing ratio with n_{in} in the haze-only regime. Results are calculated numerically based on the Eqs. 7 to 11, with $T_0 = 290$ K and $q_{v0} = 13.9$ g kg^{-1}. Blue and orange lines are for $\tau_m = 165$ s and 2000 s, respectively.

    For a given forcing (T_0, q_{v0}, and τ_m) and aerosol (r_{dry}) condition, we can calculate the equilibrium liquid water mixing ratio at the haze-only steady state by solving Eqs. 7 – 11 numerically. For a direct comparison with the above results, we set $T_0 = 290$ K, $q_{v0} = 13.9$ g kg^{-1}, and $\tau_m = 165$ s, same as those used in the box model. Figure 10 shows that q_l increases with n_{in} linearly in log-log space with a slope of about 0.83, which is steeper than that in the fast microphysics regime (0.67). Note

370   that we only simulate the haze-only regime in the subsaturated environment (i.e., when Eq. 10 is valid for RH<100%) here, and the slope should be related to the RH dependence of r_{eq} (Eq. 10). Results show that the required n_{in} to reach this haze-only

regime is extremely high, hundreds to thousands $\text{cm}^{-3}\text{s}^{-1}$, and q_l is also exceptionally high, tens to hundreds g kg^{-1}. The main reason for the high n_{in} and q_l is because a huge amount of slowly sedimenting haze particles are needed to balance the relatively strong forcing term to replenish water vapor so that $s < s_{crit}$ all the time. Such high q_l is likely unrealistic and

375 unachievable in the real chamber due to factors not considered in the model (see the following section). However, if $\tau_m = 2000$ s, implying a much weaker forcing, q_l in the haze-only regime can be less than 1 g kg^{-1} for a more realistic n_{in} (Fig. 10).

3.2.5 Impact of a haze sink

So far, the only sink for aerosol particles is activation. At high aerosol injection rates, activation is suppressed, and thus, they can accumulate when using the CL_{CCN} scheme (see black lines in Figs. 4 and 9, third row). Similarly, the sink for haze particles

380 is dominated by activation because their sedimentation speed is very small. We have shown that a chamber with subsaturated side walls can efficiently transfer cloud droplets to haze particles over time, leading to haze accumulation when using the CL_{Haze} scheme (red line in Fig. 9, third row). In reality, these unactivated particles (aerosols or haze particles) can also be lost by side walls, coagulation, sedimentation, or droplet scavenging, preventing their concentration from approaching infinity.
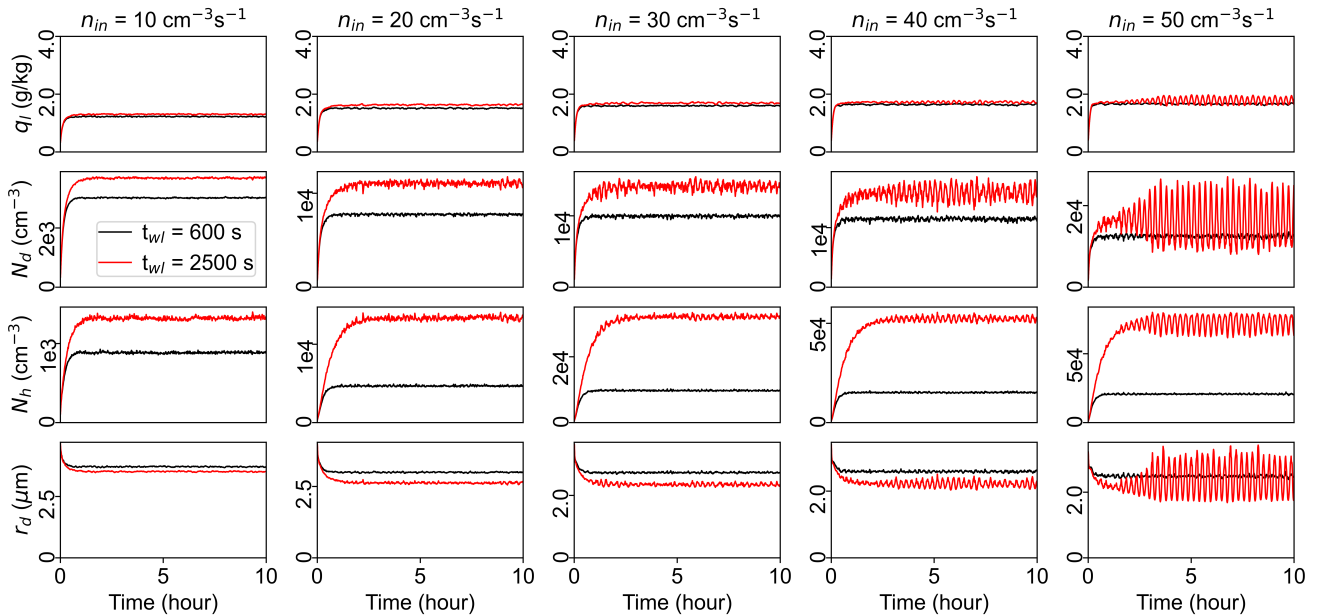
Figure 11. Similar to Fig. 4, time series of domain-averaged q_l (first row), N_d (second row), N_h (third row), and r_d (forth row) for five different n_{in}: 10, 20, 30, 40, and 50 $\text{cm}^{-3}\text{s}^{-1}$, but considering the loss of haze particles due to the side wall. Different line colors represent simulations using different wall-loss timescales (t_{wl} in Eq. 12): $t_{wl} = 600$ s (black) and 2500 s (red).

To investigate the impact of the sink of haze particles on cloud properties, especially in the cloud oscillation regime, follow-

385 ing by Thomas et al. (2023) and Wang et al. (2024) (Eq. 1 therein), a wall-loss timescale (t_{wl}) is applied to constrain N_h when

using the CL_{Haze} scheme as

$$\delta N_h = N_h \left(1 - \frac{\Delta t}{t_{wl}} \right). \tag{12}$$

Here Δt is the time step of the simulation, and δN_h is the loss of haze particles due to walls after each time step. t_{wl} is one over the particle rate loss coefficient (β) due to the walls. β can be estimated from the deposition velocity (v_{dep}) and wall area (A)

390   to volume V ratio (for the Pi chamber $A/V = 4$ m^{-1}): $\beta = v_{dep}A/V$. For simplification (i.e., neglecting the impact of other factors, such as particle size and turbulence, on v_{dep}), we set $v_{dep} = 10^{-4}$ m s^{-1}, a typical value for the deposition velocity for particles with a diameter of 2 μm (see fig. 4 in Lai, 2002), which give us $\beta = 4 \times 10^{-4}$ s^{-1} or $t_{wl} = 2500$ s. Results show that oscillation still exists for $n_{in} \geq 20$ cm^{-3}s^{-1}, but with a smaller amplitude (red line in Fig. 11). The oscillation frequency is also higher than before (compare Fig. 4 and 11 for the same n_{in}). Although we only consider the loss of haze particles

395   due to walls here, there are some other types of haze sinks, such as Brownian coagulation (Baker and Charlson, 1990) and scavenging (Sellegri et al., 2003), which might lead to a smaller effective t_{wl} in the real chamber. For another sensitivity test, we set $t_{wl} = 600$ s, the same value Thomas et al. (2019) used to constrain particle concentration for the Pi chamber simulation. Results show that the oscillation is barely seen (black line in Fig. 11). Also note that N_h increases with n_{in}, but its value is one order of magnitude smaller than before (Fig. 11 vs. 4, third row). Combined with the "cloud collapse" findings, our results

400   suggest that achieving high concentration of haze particles and synchronized activation throughout the chamber are two key factors for cloud to stay in the oscillation regime.

4 Conclusions and discussion

In this study, we conducted a series of large-eddy simulations of the Pi chamber using a haze-capable bin microphysics scheme (CL_{Haze}) developed by Yang et al. (2023) to explore haze-cloud interactions over a wide range of aerosol injection rates

405   (0.001 cm^{-3}s$^{-1} \leq n_{in} \leq 50$ cm^{-3}s^{-1}). Results are compared with simulations using a CCN-based bin microphysics scheme (CL_{CCN}). The CL_{CCN} scheme adopts a Twomey-type activation parameterization which is widely used in atmospheric cloud simulations, while the CL_{Haze} scheme can properly resolve the growth of haze particles and the activation process. Our objectives were investigating (1) the influence of different aerosol injection rates on cloud properties, and (2) the importance of haze-cloud interactions in a convection cloud chamber as well as in analogous natural cloud systems. For objective 1, we espe-

410   cially focused on the impact of n_{in} on cloud droplet number concentration (N_d), liquid water mixing ratio (q_l), and droplet size distribution, and compared results with previous analytical studies (Krueger, 2020; Shaw et al., 2023). Objective 2 is motivated by Yang et al. (2023) showing that cloud microphysical properties gained with the CL_{CCN} scheme are similar to those using the CL_{Haze} scheme, raising the question of whether we need to consider haze-cloud interactions. However, only two aerosol injection rates were investigated in Yang et al. (2023). Here, we explored the consistency of the CL_{CCN} scheme and the CL_{Haze}

415   scheme over a wider range aerosol injection rates. Low-dimensional models are also employed to explore the impact of n_{in} on cloud properties. In short, we confirm slow and fast microphysics regimes reported in previous studies (Shaw et al., 2023). We also find new microphysical regimes at high aerosol injection rates, cloud oscillation and haze-only, as illustrated in Fig. 12.
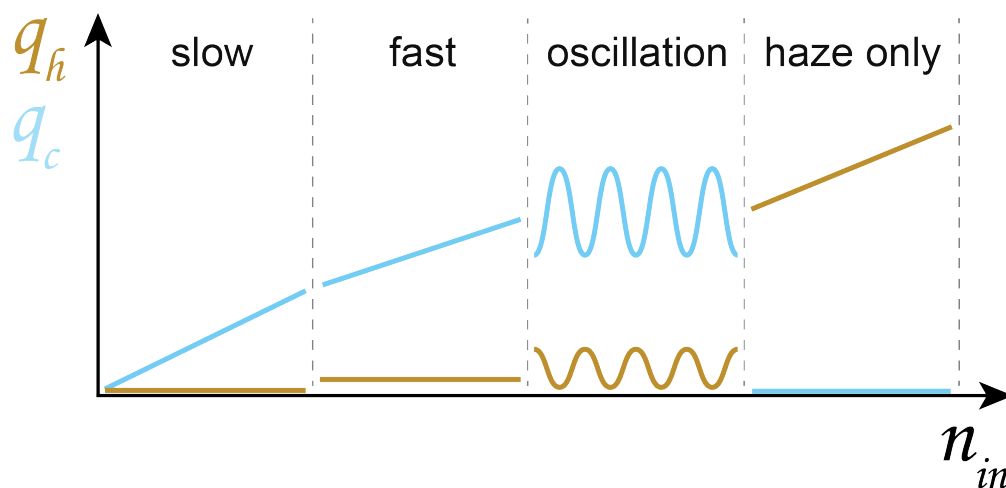
Figure 12. A schematic illustration of q_c or q_h and n_{in} relationships in different microphysics regimes: slow, fast, oscillation, and haze-only.

Slow and fast microphysics regimes were observed at small and moderate aerosol injection rates, respectively. The change of cloud properties with aerosol injection rate in these two regimes agreed with previous analytical studies (Chandrakar et al., 2020; Shaw et al., 2023). Specifically, for small aerosol injection rates ($n_{in} < 0.1$ cm^{-3}s^{-1}), the cloud was in the slow microphysics regime where droplets grow at a high supersaturation before they fall out, leading to a linear relationship between N_d and n_{in} as well as q_l and n_{in}. For moderate aerosol injection rates (0.1 cm^{-3}s$^{-1} \leq n_{in} \leq 10$ cm^{-3}s^{-1}), the cloud was in the fast microphysics regime with $N_d \sim n_{in}^{5/3}$ and $q_l \sim n_{in}^{2/3}$, consistent with the theoretical prediction in Shaw et al. (2023). In addition, droplet size distributions in the steady state became narrower and shifted to smaller sizes due to the increase in n_{in}, and the shape of the distribution also agreed reasonably well with analytical estimates (Chandrakar et al., 2020; Liu and Hallett, 1998; Krueger, 2020). But they do not capture the distribution properties at large n_{in} where haze mode is present.

The most striking phenomena are cloud oscillation, cloud collapse, and haze-only regimes occurred at high aerosol injection rates when using the CL$_{\text{Haze}}$ scheme. In contrast, cloud always reaches a steady state when using the CL$_{\text{CCN}}$ scheme. Haze-cloud interactions are responsible for the occurrence of these microphysics regimes. Specifically, cloud oscillation happened when (1) high concentration of haze particles can be achieved and (2) synchronized activation can occur throughout the chamber. In a chamber with relatively humid side walls, the supersaturation is more homogeneous in the chamber and droplets at different locations experience similar supersaturation, leading to synchronized activation ($s > s_{crit}$) or deactivation ($s < s_{crit}$) of huge number of droplets across the whole chamber – the main reason for cloud oscillation. In contrast, cloud collapse occurred when the side walls are relatively dry. Under this condition, supersaturation in the chamber is more inhomogeneous: droplets close to the side walls tend to be deactivated to haze particles while droplets away from the side walls tend to grow. The separation of droplet activation (regions close to the center, top and bottom surfaces) and deactivation (regions close to the side walls) make the chamber an efficient machine to transfer cloud droplets to haze particles – the fundamental reason for cloud collapse. The

haze-only regime occurred at extremely high aerosol injection rates. In this regime, droplet activation is totally suppressed and the formation of haze particles is balanced by their loss due to sedimentation.

440   In the real chamber, haze particles can also be removed through other mechanisms, such as wall loss and scavenging, which could constrain the haze number concentration. Therefore, clouds might struggle to achieve oscillation and haze-only regimes, especially when the source term to maintain high supersaturation is strong, e.g., large temperature difference between top and bottom surfaces, like in this study. Haze-cloud oscillation is more likely to occur under conditions of weak supersaturation forcing, e.g., small temperature difference between top and bottom surfaces in a convection chamber, or small updraft veloc-

445   ity in the real atmosphere. Recently, Gutiérrez et al. (2024) solved coupled equations for droplet growth and supersaturation development in a rising cloud parcel. Their analysis also predicts the oscillation between haze and cloud droplets under certain conditions, e.g., low air vertical velocity and high aerosol number concentration. The fundamental reason for the cloud oscillation stems from the non-linear coupled haze-cloud-supersaturation system (Arabas and Shima, 2017), and this system is analogous to other predator-prey systems observed in nature, which causes similar oscillation behaviors, such as oscillation

450   in open-cellular convection or in aerosol-cloud-precipitation system (Koren and Feingold, 2011). However, it should be mentioned that cloud oscillation reported in Gutiérrez et al. (2024) is not exactly the same as oscillation reported in this study: they only have one size of droplet/haze that varies in time, while we have coexisting haze and cloud droplets. Also note that monodisperse aerosol is used in this study, as well as in Gutiérrez et al. (2024). Aerosol particles in nature vary in size and compositions, and the impact of polydisperse aerosols on cloud microphysics regimes should be explored in the future.

455   Our results suggest that haze-cloud interactions are very important especially in polluted conditions. This is true in the Pi chamber at high aerosol injection rates as shown in this study, and it is also likely to be true in the atmosphere, for example, when cloud or fog is close to the source of intense natural and anthropogenic aerosol emissions. Studies have shown the possibility of fog consisting of just unactivated haze particles in highly polluted environment (e.g., Klemm et al., 2016). The unactivated haze particles can have important impacts on fog optical properties, such as visibility and radiation (Boutle

460   et al., 2018), as well as cloud optical properties, i.e., cloud albedo (Hoffmann et al., 2022). To properly simulate haze-cloud interactions, we need to resolve haze particles as well as the associated droplet activation and deactivation processes, instead of using Twomey-type activation parameterization.

Code and data availability. The SAM model was kindly provided by Prof. Marat Khairoutdinov of Stony Brook University and is publicly available at http://rossby.msrc.sunysb.edu/ marat/SAM.html

465   *Author contributions.* F.Y., R.A.S., and F.H.: conceptualization. F.Y., H.F.S., and A.W.: code development and debug. F.Y. and H.F.S.: conducting simulations. F.Y. and P.H.: data analysis and visualization. F.Y.: original draft preparation. H.F.S., R.A.S., F.H., P.H., A.W., and M.O., writing - review and editing.

Competing interests. The contact author has declared that none of the authors has any competing interests.

Acknowledgements. This work was supported by Office of Science Biological and Environmental Research program as part of the At-
470 mospheric Systems Research program. Brookhaven National Laboratory is operated by Battelle for the U.S. Department of Energy under
contract DE-SC0012704. PNNL is operated for the Department of Energy by Battelle Memorial Institute under Contract DE-AC05-76
RL01830. H. Fahandezh and R.A. Shaw were supported by NSF grant AGS-2133229. F.Hoffmann is supported by the German Research
Foundation (DFG) under grant HO 6588/1-1. We thank Subin Thomas, who was involved with early large eddy simulations that hinted at
the possibility of cloud oscillations. We thank Ernie Lewis for helpful discussions that made us aware of Equation 10. F. Yang also thanks
475 Kamal Kant Chandrakar and Silvio Schmalfuß for helpful discussions.

References

Anderson, J. C., Beeler, P., Ovchinnikov, M., Cantrell, W., Krueger, S., Shaw, R. A., Yang, F., and Fierce, L.: Enhancements in cloud condensation nuclei activity from turbulent fluctuations in supersaturation, Geophysical Research Letters, 50, e2022GL102 635, https://doi.org/10.1029/2022GL102635, 2023.

480 Arabas, S. and Shima, S.-i.: On the CCN (de) activation nonlinearities, Nonlinear processes in geophysics, 24, 535–542, https://doi.org/10.5194/npg-24-535-2017, 2017.

Baker, M. B. and Charlson, R. J.: Bistability of CCN concentrations and thermodynamics in the cloud-topped boundary layer, Nature, 345, 142–145, https://doi.org/10.1038/345142a0, 1990.

Boutle, I., Price, J., Kudzotsa, I., Kokkola, H., and Romakkaniemi, S.: Aerosol–fog interaction and the transition to well-mixed radiation fog,
485 Atmospheric Chemistry and Physics, 18, 7827–7840, https://doi.org/10.5194/acp-18-7827-2018, 2018.

Brown, P. N., Byrne, G. D., and Hindmarsh, A. C.: VODE: A variable-coefficient ODE solver, SIAM journal on scientific and statistical computing, 10, 1038–1051, https://doi.org/10.1137/0910062, 1989.

Chandrakar, K. K., Cantrell, W., Chang, K., Ciochetto, D., Niedermeier, D., Ovchinnikov, M., Shaw, R. A., and Yang, F.: Aerosol indirect effect from turbulence-induced broadening of cloud-droplet size distributions, Proceedings of the National Academy of Sciences, 113,
490 14 243–14 248, https://doi.org/10.1073/pnas.1612686113, 2016.

Chandrakar, K. K., Saito, I., Yang, F., Cantrell, W., Gotoh, T., and Shaw, R. A.: Droplet size distributions in turbulent clouds: Experimental evaluation of theoretical distributions, Quarterly Journal of the Royal Meteorological Society, 146, 483–504, https://doi.org/10.1002/qj.3692, 2020.

Chang, K., Bench, J., Brege, M., Cantrell, W., Chandrakar, K., Ciochetto, D., Mazzoleni, C., Mazzoleni, L., Niedermeier, D., and Shaw,
495 R.: A laboratory facility to study gas–aerosol–cloud interactions in a turbulent environment: The π chamber, Bulletin of the American Meteorological Society, 97, 2343–2358, https://doi.org/10.1175/BAMS-D-15-00203.1, 2016.

Chen, J., Liu, Y., Zhang, M., and Peng, Y.: New understanding and quantification of the regime dependence of aerosol-cloud interaction for studying aerosol indirect effects, Geophysical Research Letters, 43, 1780–1787, https://doi.org/10.1002/2016GL067683, 2016.

Chen, J.-P. and Lamb, D.: Simulation of cloud microphysical and chemical processes using a multicomponent framework. Part
500 I: Description of the microphysical model, Journal of Atmospheric Sciences, 51, 2613–2630, https://doi.org/10.1175/1520-0469(1994)051<2613:SOCMAC>2.0.CO;2, 1994.

Grabowski, W. W.: Comparison of Eulerian bin and Lagrangian particle-based schemes in simulations of Pi Chamber dynamics and microphysics, Journal of the Atmospheric Sciences, 77, 1151–1165, https://doi.org/10.1175/JAS-D-19-0216.1, 2020.

Grabowski, W. W., Morrison, H., Shima, S.-I., Abade, G. C., Dziekan, P., and Pawlowska, H.: Modeling of cloud microphysics: Can we do
505 better?, Bulletin of the American Meteorological Society, 100, 655–672, https://doi.org/10.1175/BAMS-D-18-0005.1, 2019.

Gutiérrez, M. S., Chekroun, M. D., and Koren, I.: Dynamical regimes of CCN activation in adiabatic air parcels, arxiv, https://doi.org/10.48550/arXiv.2405.11545, 2024.

Hoffmann, F., Mayer, B., and Feingold, G.: A parameterization of interstitial aerosol extinction and its application to marine cloud brightening, Journal of the Atmospheric Sciences, 79, 2849–2862, https://doi.org/10.1175/JAS-D-22-0047.1, 2022.

510 Jensen, J. B. and Nugent, A. D.: Condensational growth of drops formed on giant sea-salt aerosol particles, Journal of the atmospheric sciences, 74, 679–697, https://doi.org/10.1175/JAS-D-15-0370.1, 2017.

Khairoutdinov, M. F. and Randall, D. A.: Cloud resolving modeling of the ARM summer 1997 IOP: Model formulation, results, uncertainties, and sensitivities, Journal of the Atmospheric Sciences, 60, 607–625, https://doi.org/10.1175/1520-0469(2003)060<0607:CRMOTA>2.0.CO;2, 2003.

515 Khvorostyanov, V. I. and Curry, J. A.: Refinements to the Köhler's theory of aerosol equilibrium radii, size spectra, and droplet activation: Effects of humidity and insoluble fraction, Journal of Geophysical Research: Atmospheres, 112, https://doi.org/10.1029/2006JD007672, 2007.

Klemm, O., Lin, N., et al.: What causes observed fog trends: air quality or climate change?, Aerosol and Air Quality Research, 16, 1131–1142, https://doi.org/10.4209/aaqr.2015.05.0353, 2016.

520 Koren, I. and Feingold, G.: Aerosol–cloud–precipitation system as a predator-prey problem, Proceedings of the National Academy of Sciences, 108, 12 227–12 232, https://doi.org/10.1073/pnas.1101777108, 2011.

Korolev, A. V.: The influence of supersaturation fluctuations on droplet size spectra formation, Journal of Atmospheric Sciences, 52, 3620–3634, https://doi.org/10.1175/1520-0469(1995)052<3620:TIOSFO>2.0.CO;2, 1995.

Korolev, A. V. and Mazin, I. P.: Supersaturation of water vapor in clouds, Journal of the atmospheric sciences, 60, 2957–2974, 525 https://doi.org/10.1175/1520-0469(2003)060<2957:SOWVIC>2.0.CO;2, 2003.

Krueger, S. K.: Equilibrium droplet size distributions in a turbulent cloud chamber with uniform supersaturation, Atmospheric Chemistry and Physics, 20, 7895–7909, https://doi.org/10.5194/acp-20-7895-2020, 2020.

Lai, A.: Particle deposition indoors: a review., Indoor air, 12, 211–214, https://doi.org/10.1034/j.1600-0668.2002.01159.x, 2002.

Lehmann, K., Siebert, H., and Shaw, R. A.: Homogeneous and inhomogeneous mixing in cumulus clouds: Dependence on local turbulence 530 structure, Journal of the Atmospheric Sciences, 66, 3641–3659, https://doi.org/10.1175/2009JAS3012.1, 2009.

Lewis, E. R.: The dependence of radius on relative humidity and solute mass at high relative humidities up to and including 100%, Journal of Geophysical Research: Atmospheres, 124, 2105–2126, https://doi.org/10.1029/2018JD030008, 2019.

Liu, Y. and Hallett, J.: On size distributions of cloud droplets growing by condensation: A new conceptual model, Journal of the atmospheric sciences, 55, 527–536, https://doi.org/10.1175/1520-0469(1998)055<0527:OSDOCD>2.0.CO;2, 1998.

535 MacMillan, T., Shaw, R. A., Cantrell, W. H., and Richter, D. H.: Direct numerical simulation of turbulence and microphysics in the Pi Chamber, Physical Review Fluids, 7, 020 501, https://doi.org/10.1103/PhysRevFluids.7.020501, 2022.

McGraw, R. and Liu, Y.: Brownian drift-diffusion model for evolution of droplet size distributions in turbulent clouds, Geophysical research letters, 33, https://doi.org/10.1029/2005GL023545, 2006.

Monin, A. and Obukhov, A.: Basic laws of turbulent mixing in the atmosphere near the ground, Tr. Geofiz. Inst., Akad. Nauk SSSR, 24, 540 163–187, 1954.

Morrison, H., Witte, M., Bryan, G. H., Harrington, J. Y., and Lebo, Z. J.: Broadening of modeled cloud droplet spectra using bin microphysics in an Eulerian spatial domain, Journal of the Atmospheric Sciences, 75, 4005–4030, https://doi.org/10.1175/JAS-D-18-0055.1, 2018.

Morrison, H., van Lier-Walqui, M., Fridlind, A. M., Grabowski, W. W., Harrington, J. Y., Hoose, C., Korolev, A., Kumjian, M. R., Milbrandt, J. A., Pawlowska, H., et al.: Confronting the challenge of modeling cloud and precipitation microphysics, Journal of advances in modeling 545 earth systems, 12, e2019MS001 689, https://doi.org/10.1029/2019MS001689, 2020.

Prabhakaran, P., Shawon, A. S. M., Kinney, G., Thomas, S., Cantrell, W., and Shaw, R. A.: The role of turbulent fluctuations in aerosol activation and cloud formation, Proceedings of the National Academy of Sciences, 117, 16 831–16 838, https://doi.org/10.1073/pnas.2006426117, 2020.

Prabhakaran, P., Thomas, S., Cantrell, W., Shaw, R. A., and Yang, F.: Sources of stochasticity in the growth of cloud droplets: Supersaturation fluctuations versus turbulent transport, Journal of the Atmospheric Sciences, 79, 3145–3162, https://doi.org/10.1175/JAS-D-22-0051.1, 2022.

Saito, I., Gotoh, T., and Watanabe, T.: Broadening of cloud droplet size distributions by condensation in turbulence, Journal of the Meteorological Society of Japan. Ser. II, 97, 867–891, https://doi.org/10.2151/jmsj.2019-049, 2019.

Sellegri, K., Laj, P., Dupuy, R., Legrand, M., Preunkert, S., and Putaud, J.-P.: Size-dependent scavenging efficiencies of multicomponent atmospheric aerosols in clouds, Journal of Geophysical Research: Atmospheres, 108, https://doi.org/10.1029/2002JD002749, 2003.

Shaw, R. A., Thomas, S., Prabhakaran, P., Cantrell, W., Ovchinnikov, M., and Yang, F.: Fast and slow microphysics regimes in a minimalist model of cloudy Rayleigh-Bénard convection, Physical Review Research, 5, 043 018, https://doi.org/10.1103/PhysRevResearch.5.043018, 2023.

Thomas, S., Ovchinnikov, M., Yang, F., van der Voort, D., Cantrell, W., Krueger, S. K., and Shaw, R. A.: Scaling of an atmospheric model to simulate turbulence and cloud microphysics in the Pi Chamber, Journal of Advances in Modeling Earth Systems, 11, 1981–1994, https://doi.org/10.1029/2019MS001670, 2019.

Thomas, S., Yang, F., Ovchinnikov, M., Cantrell, W., and Shaw, R. A.: Scaling of turbulence and microphysics in a convection–cloud chamber of varying height, Journal of Advances in Modeling Earth Systems, 15, e2022MS003 304, https://doi.org/10.1029/2022MS003304, 2023.

Twomey, S.: The nuclei of natural cloud formation part II: The supersaturation in natural clouds and the variation of cloud droplet concentration, Geofisica pura e applicata, 43, 243–249, https://doi.org/10.1007/BF01993560, 1959.

Wang, A., Yang, X. I. A., and Ovchinnikov, M.: An investigation of LES wall modeling for Rayleigh-Bénard convection via interpretable and physics-aware feedforward neural networks with DNS, Journal of the Atmospheric Sciences, https://doi.org/https://doi.org/10.1175/JAS-D-23-0094.1, 2023.

Wang, A., Ovchinnikov, M., Yang, F., Shaw, R. A., and Schmalfuss, S.: Designing a convective cloud chamber for collision coalescence using atmospheric large-eddy simulation with bin microphysics scheme, Journal of Advances in Modeling Earth Systems, 16, https://doi.org/10.1029/2023MS003734, 2024.

Xue, H. and Feingold, G.: A modeling study of the effect of nitric acid on cloud properties, Journal of Geophysical Research: Atmospheres, 109, https://doi.org/10.1029/2004JD004750, 2004.

Yang, F., Shaw, R., and Xue, H.: Conditions for super-adiabatic droplet growth after entrainment mixing, Atmospheric Chemistry and Physics, 16, 9421–9433, https://doi.org/10.5194/acp-16-9421-2016, 2016.

Yang, F., Kollias, P., Shaw, R. A., and Vogelmann, A. M.: Cloud droplet size distribution broadening during diffusional growth: ripening amplified by deactivation and reactivation, Atmospheric Chemistry and Physics, 18, 7313–7328, https://doi.org/10.5194/acp-18-7313-2018, 2018.

Yang, F., Ovchinnikov, M., Thomas, S., Khain, A., McGraw, R., Shaw, R. A., and Vogelmann, A. M.: Large-eddy simulations of a convection cloud chamber: Sensitivity to bin microphysics and advection, Journal of Advances in Modeling Earth Systems, 14, e2021MS002 895, https://doi.org/10.1029/2021MS002895, 2022.

Yang, F., Hoffmann, F., Shaw, R. A., Ovchinnikov, M., and Vogelmann, A. M.: An intercomparison of large-eddy simulations of a convection cloud chamber using haze-capable bin and Lagrangian cloud microphysics schemes, Journal of Advances in Modeling Earth Systems, 15, e2022MS003 270, https://doi.org/10.1029/2022MS003270, 2023.

Yau, M. K. and Rogers, R. R.: A short course in cloud physics, Elsevier, 1996.